Supplementary Information for

Advancing Agrivoltaics through a Systematic Design Framework: Guidelines for Integration and Informed Decision-Making

Xuzhi Du[1,*], Alexandra Solecki[1], Muhammad Jahidul Hoque[1], Vivek S. Garimella[1], Mengqi Jia[2], Bin Peng[2,3], Paul Mwebaze[2], James McCall[4], Fahd Majeed[2], Alson Time[2], Jinwook Kim[2], Matthew Sturchio[5], Kaiyu Guan[2,6], Madhu Khanna[2], Carl J Bernacchi[2,7], DoKyoung Lee[2], Alan K Knapp[5], Greg A Barron-Gafford[8], Bruce Branham[3], Nenad Miljkovic[1,2,9,10,11,*]

[1]*Mechanical Science and Engineering, University of Illinois at Urbana-Champaign, Urbana, IL 61801, USA*

[2]*Institute for Sustainability, Energy, and Environment, University of Illinois Urbana-Champaign, Urbana, IL 61801, USA*

[3]*Department of Crop Sciences, College of Agricultural, Consumer, and Environmental Sciences, University of Illinois Urbana-Champaign, Urbaba, IL 61801, USA*

[4]*National Renewable Energy Laboratory, Golden, CO, USA*

[5]*Department of Biology, Colorado State University, CO, USA*

[6]*Department of Natural Resources and Environmental Sciences, College of Agricultural, Consumer, and Environmental Sciences, University of Illinois Urbana-Champaign, Urbaba, IL 61801, USA*

[7]*Global Change and Photosynthesis Research Unit, USDA-ARS, Urbana, IL, USA*

[8]*School of Geography, Development & Environment, University of Arizona, AZ, USA*

[9]*Department of Electrical and Computer Engineering, University of Illinois, Urbana, IL 61801, USA*

[10]*Materials Research Laboratory, University of Illinois, Urbana, IL 61801, USA*

[11]*International Institute for Carbon Neutral Energy Research (WPI-I2CNER), Kyushu University, 744 Moto-oka, Nishi-ku, Fukuoka 819-0395, Japan*

***Correspondence**: xuzhidu@illinois.edu, nmiljkov@illinois.edu

This file includes:

Supplementary Notes 1-4

Supplementary Figures 1-14

Supplementary Tables 1-2

Supplementary References

Note: All Python files will be uploaded to a public repository Zenodo. The repository link is: https://zenodo.org/

Supplementary Notes

Supplementary Note 1

Solar model. Supplementary Figure 13 illustrates the PV module's orientation in relation to the sun. Solar position is articulated through the zenith angle (θ_z) and solar azimuth angle (θ_{sa}). θ_z represents the angle between the sun's rays and the vertical direction, serving as the complement to solar altitude or elevation[1–3]. θ_{sa} signifies the angle between the projection of sun rays and a line due north or south[4], measured on the horizontal plane. Both θ_z and θ_{sa} are dynamic parameters influenced by local coordinates (latitude and longitude) and time, which is calculated using the NREL's algorithm implemented in Sandia's photovoltaic modeling library (PVLib)[5,6]. In addition to PV array density and PV panel height, the panel tilt angle (θ_t) and panel azimuth angle (θ_{pa}) are pivotal in describing the PV panel orientation. Specifically, θ_t represents the angle between the horizontal plane and the PV panel, while θ_{pa} is the horizontal orientation in relation to the north direction, typically measured clockwise from true north. In the case of fixed PV panels, θ_t and θ_{pa} are typically set at optimal values to maximize PV generation based on the solar farm's location. However, if PV panels are configured in a tracking scheme for enhanced PV generation, both θ_t and θ_{pa} undergo dynamic variations.

In this context, the angle of incidence (θ_{AOI}) between sunlight and the PV panel front surface can be expressed as:

$$\cos(\theta_{AOI}) = \boldsymbol{S} \cdot \boldsymbol{N}\,, \tag{S1}$$

where $\boldsymbol{S}$ is the unit vector of solar rays and $\boldsymbol{N}$ is the unit vector normal of the PV panel surface. According to Supplementary Figure 13a, $\boldsymbol{S}$ and $\boldsymbol{N}$ can be calculated by:

$$\boldsymbol{S} = \cos(\theta_z)\,\hat{\boldsymbol{z}} + \sin(\theta_z)\sin(\theta_{sa})\hat{\boldsymbol{e}} + \sin(\theta_z)\cos(\theta_{sa})\,\hat{\boldsymbol{n}}\,, \tag{S2}$$

$$\boldsymbol{N} = \cos(\theta_t)\hat{\boldsymbol{z}} + \sin(\theta_t)\sin(\theta_{pa})\hat{\boldsymbol{e}} + \sin(\theta_t)\cos(\theta_{pa})\hat{\boldsymbol{n}}\ , \tag{S3}$$

where $\hat{\boldsymbol{z}}$, $\hat{\boldsymbol{e}}$ and $\hat{\boldsymbol{n}}$ represent unit vectors pointing vertically, eastward, and northward, respectively. Hence, θ_{AOI} can be derived as:

$$\cos(\theta_{AOI}) = \cos(\theta_z)\cos(\theta_t) + \sin(\theta_z)\sin(\theta_t)\cos(\theta_{pa} - \theta_{sa})\ . \tag{S4}$$

Typically, the potential direct solar irradiance reaching the PV panel ($I_{PV,dir}^{pot}$), accounting for the largest portion of PV generation, can be calculated by:

$$I_{PV,dir}^{pot} = I_{DNI} \cdot \cos(\theta_{AOI})\ , \tag{S5}$$

where I_{DNI} is the direct normal solar irradiance. Hence, we can achieve the maximum $I_{PV,dir}^{pot}$ by differentiating $I_{PV,dir}^{pot}$ with respect to the tilt angle and set it equal to zero:

$$\frac{\partial I_{PV,dir}^{pot}}{\partial \theta_{AOI}} = 0\ . \tag{S6}$$

Furthermore, we can obtain the critical panel tilt angle, also considered as the dynamic tracking angle ($\theta_{t,tra}$) for the classical single-axis tracking scheme[7]:

$$\theta_{t,tra} = \tan^{-1}[\tan(\theta_z)\cos(\theta_{pa} - \theta_{sa})]\ . \tag{S7}$$

Based on equations (S4) - (S7), the minimum $\theta_{AOI,min}$ and the maximum $I_{PV,dir,max}^{pot}$ can be derived as:

$$\theta_{AOI,min} = \cos^{-1}[\cos(\theta_z)\cos(\theta_{t,tra}) + \sin(\theta_z)\sin(\theta_{t,tra})\cos(\theta_{pa} - \theta_{sa})]\ , \tag{S8}$$

$$I_{PV,dir,max}^{pot} = I_{DNI} \cdot \cos(\theta_{AOI,min})\ . \tag{S9}$$

In addition, leveraging equations (S8) and (S9), along with the solar position[5,6] and PV panel specifications (Supplementary Note 1 and Supplementary Table 1), enables us to obtain analytical solutions for solar irradiance distribution on and under the PV panels.

For the collection of solar irradiance on PV panels, we make the assumption that PV panels have sufficient length to neglect edge effects on PV generation[8,9]. Typically, PV generation comprises three fundamental components: direct ($I_{PV,dir}$), diffused ($I_{PV,dif}$) and albedo ($I_{PV,alb}$) solar irradiance collections (Supplementary Figure 11b-e).

The direct solar irradiance collection ($I_{PV,dir}$, Supplementary Figure 13b) can be calculated by:

$$I_{PV,dir}(l) = \begin{cases} I_{DNI} \cdot \cos(\theta_{AOI}) \cdot \left(1 - R(\theta_{AOI})\right) \cdot \eta_{dir}, & (l > h_s) \\ 0, & (l \leq h_s) \end{cases}, \tag{S10}$$

where $R(\theta_{AOI})$ is the angle-dependent reflectivity of the panel[9], and η_{dir} is the PV module efficiency for direct irradiance[9–11]. The shade length on the panel due to the blockage of direct sunlight by adjacent panels is denoted as h_s (Supplementary Figure 13f). Assuming zero contribution from the shaded area, the average direct sunlight collection per unit panel area ($I_{PV.dir}$) can be further derived as:

$$\begin{aligned} I_{PV,dir} &= \frac{1}{h}\int_0^h \left(I_{DNI} \cdot \cos(\theta_{AOI})\left(1 - R(\theta_{AOI})\right) \cdot \eta_{dir}\right) dl \\ &= \frac{h - h_s}{h} \cdot I_{DNI} \cdot \cos(\theta_{AOI})\left(1 - R(\theta_{AOI})\right) \cdot \eta_{dir} . \end{aligned} \tag{S11}$$

The diffused sunlight collection component ($I_{PV,dif}$, Supplementary Figure 13c) is more complex than $I_{PV,dir}$ and can be expressed as:

$$I_{PV,dif} = I^F_{PV,dif} + I^B_{PV,dif} , \tag{S12}$$

where $I^F_{PV,dif}$ and $I^B_{PV,dif}$ represent the average diffused sunlight collection per unit area of a bifacial PV panel (considering both front and back surfaces). For an observation point (l) on the front surface, the diffused sunlight collection is given by:

$$I^F_{PV,dif}(l) = I_{DHI} \cdot F_{dif,PV-sky}(l) \cdot \eta_{dif} , \tag{S13}$$

where I_{DHI} is the diffused horizontal solar irradiance, $F_{dif,PV-sky}(l)$ is the view factor from the observation point (l) to the unobstructed sky, and η_{dif} is the PV module efficiency for diffused irradiance. Here, $F_{dif,PV-sky}(l)$ can be calculated by[9]:

$$F_{dif}(l) = I_{DHI} \cdot \frac{1}{2}\left(1 + \cos(\theta_t + \varphi_{m,PV-PV}(l))\right) \cdot \eta_{dif} \,, \tag{S14}$$

$$\varphi_{PV,m}(l) = \tan^{-1}\left[\frac{(h-l)\sin(\theta_t)}{p-(h-l)\cos(\theta_t)}\right], \tag{S15}$$

where $\varphi_{m,PV-PV}(l)$ is the mask angle from the observation point (l) to the adjacent panel, and p is the row-to-row PV spacing (Supplementary Figure 13c). Hence, the average diffused sunlight collection per unit area of a bifacial PV panel ($I_{PV,dif}$) can be further derived as:

$$I_{PV,dif}^{F} = \frac{I_{DHI}\eta_{dif}}{h} \int_0^h \left(\frac{1}{2}\left(1 + \cos(\theta_t + \varphi_{m,PV-PV}(l))\right)\right) dl \,. \tag{S16}$$

A similar calculation scheme was applied to the back surface of the panel where the tilt angle become $180° - \theta_t$. Finally, the total diffused sunlight collection per unit bifacial panel area ($I_{PV,dif}$) equals the sum of the front surface component ($I_{PV,dif}^{F}$) and the back surface component ($I_{PV,dif}^{B}$).

Compared with the direct ($I_{PV,dir}$) and diffused ($I_{PV,dif}$) components, the albedo sunlight collection ($I_{PV,alb}$) can be the most complex due to the albedo calculation process. $I_{PV,alb}$ includes direct and diffused albedo sunlight collections (Supplementary Figure 11d,e):

$$I_{PV,alb} = I_{PV,alb,dir}^{F} + I_{PV,alb,dir}^{B} + I_{PV,alb,dif}^{F} + I_{PV,alb,dif}^{B} \,, \tag{S17}$$

where $I_{PV,alb,dir}^{F}$ and $I_{PV,alb,dir}^{B}$ are the direct albedo sunlight collected on the front and back surfaces of the panel, respectively. $I_{PV,alb,dif}^{F}$ and $I_{PV,alb,dif}^{B}$ are the diffused albedo sunlight collected on the front and back surfaces of the panel, respectively. Here, $I_{PV,alb,dir}^{F}$ can be calculated by:

$$I_{PV,alb,dir}^{F} = \frac{1}{h} \int_0^h I_{gnd,dir} \cdot R_A \cdot F_{alb,dir,PV-gnd}^{F}(l) \cdot \eta_{dif} dl \,, \tag{S18}$$

where $I_{gnd,dir}$ is the direct solar irradiance on the ground, R_A represent the ground albedo[12] and

104 $F^{F}_{alb,dir,PV-gnd}(l)$ denotes the view factor from the observation point (l) on the panel to the

105 unshaded zone on the ground. $F^{F}_{alb,dir,PV-gnd}(l)$ can be expressed as[8,9]:

$$F^{F}_{alb,dir,PV-gnd}(l) = \sum_i \frac{1}{2}\{[\sin(\varphi^{i}_{alb,dir,2}) - \sin(\varphi^{i}_{alb,dir,1})] + [\sin(\varphi^{i}_{alb,dir,4}) - \sin(\varphi^{i}_{alb,dir,3})]\}, \quad \text{(S19)}$$

$$\varphi^{i}_{alb,dir,1} = \pi - \theta_t - \tan^{-1}\left[\frac{-x_{l,ts}+(i-1)p+\frac{E+l\sin(\theta_t)}{\tan(\theta_t)}}{E+l\sin(\theta_t)}\right], \quad \text{(S20)}$$

$$\varphi^{i}_{alb,dir,2} = \pi - \theta_t - \tan^{-1}\left[\frac{(i-1)p+\frac{E+l\sin(\theta_t)}{\tan(\theta_t)}}{E+l\sin(\theta_t)}\right], \quad \text{(S21)}$$

$$\varphi^{i}_{alb,dir,3} = \pi - \theta_t - \tan^{-1}\left[\frac{-x_{l,bs}+(i-1)p+\frac{E+l\sin(\theta_t)}{\tan(\theta_t)}}{E+l\sin(\theta_t)}\right], \quad \text{(S22)}$$

$$\varphi^{i}_{alb,dir,4} = \pi - \theta_t - \tan^{-1}\left[\frac{ip+\frac{E+l\sin(\theta_t)}{\tan(\theta_t)}}{E+l\sin(\theta_t)}\right], \quad \text{(S23)}$$

106 where E represents the height between the bottom edge of the panel and ground, and $x_{l,ts}$ and

107 $x_{l,bs}$ denote the shade edges formed by the top and bottom edges of the PV panel, respectively. A

108 similar calculation scheme was employed for the back surface of the PV panel. Additionally,

109 $I^{F}_{PV,alb,dif}$ can be expressed as (Supplementary Figure 13e):

$$I^{F}_{PV,alb,dif} = \frac{1}{h}\int_0^h I_{gnd,dif} \cdot R_A \cdot F^{F}_{alb,dif,PV-gnd}(l) \cdot \eta_{dif} dl, \quad \text{(S24)}$$

110 where $I_{gnd,dif}$ represents the diffused solar irradiance on the ground, and $F^{F}_{alb,dif,PV-gnd}(l)$

111 denotes the view factor from the observation point (l) on the panel to the ground. Here,

112 $F^{F}_{alb,dif,PV-gnd}(l)$ can be calculated by[8,9]:

$$F^{F}_{alb,dif,PV-gnd}(l) = \frac{1}{2}[1 - \sin(\varphi_{alb,dif})], \quad \text{(S25)}$$

$$\varphi_{alb,dif} = \begin{cases} \frac{\pi}{2} - \theta_t + \tan^{-1}\left(\frac{E+l\sin(\theta_t)}{\frac{E+l\sin(\theta_t)}{\tan(\theta_t)}+ip}\right), & \text{if } ip \le x_b \\ \frac{\pi}{2} - \theta_t + \tan^{-1}\left(\frac{E+l\sin(\theta_t)}{\frac{E+l\sin(\theta_t)}{\tan(\theta_t)}+x_b}\right), & \text{if } ip > x_b \end{cases}, \tag{S26}$$

where $\varphi_{alb,dif}$ signifies the view angle from the observation point (l) to the ground, and x_b denotes the intersection point of the block line and along the x-axis. A similar calculation scheme was applied to the back surface of the panel, considering both $I^B_{PV,alb,dir}$ and $I^B_{PV,alb,dif}$.

Based on equations (S4) - (S26), the total average sunlight collection per unit bifacial PV panel area ($I_{PV,aver}$) can be expressed as:

$$I_{PV,aver} = I_{PV,dir} + I_{PV,dif} + I_{PV,alb}\ . \tag{S27}$$

As the cell temperature significantly influences PV generation, we employ the Faiman model[13–15] and NREL's PVWatts DC power model[16] to establish the correlation between real climatic conditions and PV generation. Here, the alternating current (AC) power of a PV panel can be expressed as:

$$P_{AC} = \frac{I_{PV,aver}}{1000} P_{DC0}\left[1 + \gamma_{PDC}\left(T_{cell} - T_{ref}\right)\right] \cdot \mathrm{ILR} \cdot n_m, \tag{S28}$$

where P_{DC0} is the nominal direct current (DC) power of the PV module under standard test conditions (STC) of 1000 $\mathrm{W/m^2}$ and cell temperature of 25 °C, γ_{PDC} is the temperature coefficient of power (typically ranging from -0.002 /°C to -0.005 /°C), T_{cell} is the cell temperature, T_{ref} is the cell reference temperature (25 °C), ILR is the inverter loading ratio[17], and n_m is the number of PV modules in a PV panel. According to the Faiman model[13–15], T_{cell} can be calculated by:

$$T_{cell} = T_{air} + \frac{q_{store}}{f_{tot,loss}}, \tag{S29}$$

where T_{air} is the air temperature, q_{store} is the net heat flux stored within PV cells, and $f_{tot,loss}$

is the total loss factor. Here, q_{store} and $f_{tot,loss}$ can be expressed as:

$$q_{store} = I_{PV,aver} - q_{rad-sky} \,, \tag{S30}$$

$$q_{rad-sky} = \varepsilon_{PV} \cdot F_{dif,PV-sky} \cdot \sigma \cdot (T_{air} - T_{abs,zero})^4, \tag{S31}$$

$$f_{tot,loss} = u_0 + u_1 \cdot v_{wind} \,, \tag{S32}$$

where $q_{rad-sky}$ represents the heat loss from PV module surface to the sky due to radiation, ε_{PV} is the infrared emissivity of the PV module surface facing the sky, σ is the Stefan-Boltzmann constant (5.67×10^{-8} W/(m^2·K^4)), $T_{abs,zero}$ is the absolute zero temperature (-273.15 K), u_0 is the combined heat loss factor coefficient, u_1 is the combined heat loss factor influenced by the local wind, and v_{wind} is the local wind speed measured at the same height of the PV module which can be extracted directly from the National Solar Radiation Database (NSRDB)[18–23].

The solar irradiance intercepted by PAR available to the crops under PV panels can significantly influence crop growth[24]. We commence by calculating the spatial shade distribution, where the blockage of direct solar irradiance by PV panels creates shade on the ground or at any elevation below the PV arrays. The length (l_s) and the edges (l_{ts}, l_{bs}) of the shade (Supplementary Figure 13f) are determined by:

$$l_s = l_{ts} - l_{bs} \,, \tag{S33}$$

$$l_{ts} = \frac{E + h\sin(\theta_t)}{\tan(\theta_t)} + \frac{[E + h\sin(\theta_t)][\cos(\theta_{pa} - \theta_{sa})]}{\tan(\frac{\pi}{2} - \theta_z)} \,, \tag{S34}$$

$$l_{bs} = \frac{E}{\tan(\theta_t)} + \frac{E[\cos(\theta_{pa} - \theta_{sa})]}{\tan(\frac{\pi}{2} - \theta_z)} \,, \tag{S35}$$

where l_{ts} and l_{bs} represent the edges of the shade caused by the top and bottom edges of the PV panel, respectively. It is essential to highlight the potential occurrence of mutual (row-to-row) shading (h_s), particularly when θ_z is low and θ_t is high (Supplementary Figure 13f). In such cases, h_s can be derived as:

$$h_s = \frac{(l_{ts} - p)[h + \frac{E}{\sin(\theta_t)}]}{l_{ts}} - \frac{E}{\sin(\theta_t)} \,. \tag{S36}$$

Usually, mutual shading can lead to significant PV production loss due to electrical mismatch[25–27]. To reduce the mutual shade influence, PV panels should operate at increased θ_{AOI} when the sun is low, preventing row-to-row shading. We employed the backtracking algorithm by rotating the tracker backward from the ideal rotation to shorten the shade cast by the PV panels and avoid shading the panels behind them. Hence, we should ensure:

$$h_s \leq 0 \,. \tag{S37}$$

Thus, based on equations (S33) - (S37), we can determine the optimum tracking scheme to maximize the potential direct solar irradiance collection.

For an arbitrary observation point (x) on the ground or at any elevation under the PV panel (Supplementary Figure 13g), local direct solar irradiance $I_{gnd,dir}(x)$ on the horizontal plane can be calculated by:

$$I_{gnd,dir}(x) = \begin{cases} I_{DNI} \cdot \cos(\theta_z), \ \text{if } x < l_{bs} \text{ or } \ x > l_{ts} \\ 0, \ \text{if } l_{ts} \leq x \leq l_{bs} \end{cases} . \tag{S38}$$

Local diffused solar irradiance $I_{gnd,dif}(x)$ on the horizontal plane can be determined by:

$$I_{gnd,dif}(x) = I_{DHI} \cdot F_{dif,gnd-sky}(x) \,, \tag{S39}$$

where I_{DHI} is the diffused horizontal solar irradiance, and $F_{gnd.dif}(x)$ is the view factor from the observation point to the unobstructed sky. Here, the calculation of $F_{gnd,dif}(x)$ is required to consider the mask angle caused by both the back and front surfaces of all PV panels (Supplementary Figure 13g). The mask angle subtended from x to the top and bottom edges of a PV panel at the back surface ($\theta^i_{t|B}$ and $\theta^i_{b|B}$) and front surface ($\theta^i_{t|F}$ and $\theta^i_{b|F}$) can be expressed as:

$$\theta_{t|B}^{i} = \begin{cases} \tan^{-1}\left[\frac{E+h\sin(\theta_t)}{-(i-1)p-x+\frac{E+h\sin(\theta_t)}{\tan(\theta_t)}}\right], & \text{if } \theta_{t|B}^{i} < \frac{\pi}{2} \\ \pi + \tan^{-1}\left[\frac{E+h\sin(\theta_t)}{-(i-1)p-x+\frac{E+h\sin(\theta_t)}{\tan(\theta_t)}}\right], & \text{if } \theta_{t|B}^{i} > \frac{\pi}{2} \end{cases}, \tag{S40}$$

$$\theta_{b|B}^{i} = \begin{cases} \tan^{-1}\left[\frac{E}{-(i-1)p-x+\frac{E}{\tan(\theta_t)}}\right], & \text{if } \theta_{t|B}^{i} < \frac{\pi}{2} \\ \pi + \tan^{-1}\left[\frac{E}{-(i-1)p-x+\frac{E}{\tan(\theta_t)}}\right], & \text{if } \theta_{t|B}^{i} > \frac{\pi}{2} \end{cases}, \tag{S41}$$

$$\theta_{t|F}^{i} = \tan^{-1}\left[\frac{E+h\sin(\theta_t)}{ip-x+\frac{E+h\sin(\theta_t)}{\tan(\theta_t)}}\right], \tag{S42}$$

$$\theta_{b|F}^{i} = \tan^{-1}\left[\frac{E}{ip-x+\frac{E}{\tan(\theta_t)}}\right]. \tag{S43}$$

Hence, the effective view factor $F_{gnd.dif}(x)$ from the observation point to the sky over all PV panels can be calculated by:

$$I_{gnd,dif}(x) = \frac{1}{2}\left[\cos\left(\sum_i(\theta_{t|B}^{i} - \theta_{b|B}^{i}\right) + \cos\left(\sum_i\left(\theta_{t|F}^{i} - \theta_{b|F}^{i}\right)\right]. \tag{S44}$$

Finally, an arbitrary observation point (x) on the ground or at any elevation under the PV panel receives the total solar irradiance:

$$I_{gnd,tot}(x) = I_{gnd,dir}(x) + I_{gnd,dif}(x), \tag{S45}$$

where the $I_{gnd,dir}(x)$ is equal to zero within the shade zone.

Validation of the solar model. To validate our solar model, we conducted solar tests at Solar Farm 2.0, focusing on solar irradiance distribution under the PV arrays (Supplementary Figure 1). Solar Farm 2.0, a 54-acre, 12.3 megawatt (MWdc) solar farm located in Champaign, Illinois (40.0692° N, 88.2481° W), is approved by the University of Illinois Board of Trustees as the sole member of Prairieland Energy, Inc. The installation features bi-facial monocrystalline PV panels with an east-west tracking system, moving daily to follow the sun's trajectory. Each PV panel, consisting of 78 PV modules (each with a length h of 2.022 m and a width w of 0.992 m), is installed with a row-to-row spacing (pitch) of ~ 5.44 m. Supplementary Figure 1c depicts the experimental setup for measuring the Photosynthetically Active Radiation (PAR) distribution under PV panels. Eight spectrometers (STS-VIS, $\pm 2\%$, Ocean Insight), evenly spaced at intervals (d_{h1}) of 0.39 m and a height (d_{v1}) of 0.84 m under the PV panel, were strategically placed for dynamic PAR distribution capture from August 3 to October 17, 2023. Additionally, we positioned an extra spectrometer beyond the confines of the solar farm to record the unobstructed sunlight, serving as a baseline for assessing shading effects. The STS-VIS spectrometer, leveraging a unique optical design and a CMOS array detector, delivers a high signal-to-noise ratio (>1500:1) and a wide dynamic range (4600:1), making it suitable for measuring low-concentration absorption to high-intensity light and laser characterization. We meticulously designed and crafted precision sensor housings using 3D printing, aiming to streamline sensor installation and enhance waterproof functionality. To enhance the scope of our experiments, we additionally utilized three quantum sensors (SQ-215-SS, $\pm 5\%$, Apogee Instruments) for PAR (400-700 nm) measurement from June 21 to September 19, 2023. The quantum sensors were installed at horizontal distances of $d_{h2} = 1.20$ m and $d_{h3} = 1.52$ m, and a vertical distance of $d_{v2} = 0.69$ m, as depicted in Supplementary Figure 1c. Similar to the spectrometer setup, we placed an additional quantum sensor outside the solar farm to capture the unobstructed sunlight, thus facilitating a detailed analysis of shade levels.

Supplementary Figure 1d illustrates the comparison of solar irradiance distribution between simulation and test results. Due to the NSRDB database[18–23] being updated only until the year 2022, we performed the simulation using the real weather data from the last decade (2013-2022) to achieve the time-averaged spatial solar irradiance distribution, which corresponds to the test periods. To enable an equitable comparison, we normalized both the simulated and observed local solar irradiances against full sunlight measurements outside the solar farm. we also nondimensionalized the observation position x relative to the PV length (h). We observe a high level of consistency between the simulation results and the experimental outcomes. This indicates that our solar model can dynamically capture the spatial PAR distribution under PV panels with a high fidelity. In addition to the validation of PAR distribution, we conducted a comparative study of PV generation between our solar model and meter readings from Solar Farm 2.0, as illustrated in Supplementary Figure 1b. Likewise, our solar model demonstrates a remarkable ability to predict the PV generation of Solar Farm 2.0, with most discrepancies being less than 6%. This robust performance establishes a solid foundation for developing the AV system design model.

Supplementary Note 2

Crop model. Here, the model simulated soybean yield ($Y_{crop,AV}$) as:

$$Y_{crop,AV} = \Delta Q_r \times \mathrm{HI}\,, \tag{S46}$$

where ΔQ_r represents the radiation-limited dry-biomass accumulation, and HI denotes the harvest index. Here, ΔQ_r is a function of the intercepted radiation (I), radiation use efficiency (RUE), diffuse factor (f_d), stress factor (f_s), and carbon dioxide factor (f_c):

$$\Delta Q_r = I \times \mathrm{RUE} \times f_d \times f_s \times f_c\,. \tag{S47}$$

Here, the intercepted radiation (I) can be calculated based on the leaf area index (LAI, $\mathrm{m^2/m^2}$) and the extinction coefficient k[28–30]:

$$I = I_0\left(1 - \frac{\exp(-k \times \mathrm{LAI} \times f_h)}{f_h}\right), \tag{S48}$$

where I_0 signifies the total radiation at the top of the canopy (MJ), and f_h is light interception modified to give hedge-row effect with skip row, which is set to 1 according to the APSIM soybean model[28,29]. The leaf area index (LAI), a key factor in carbon production, is determined by the increase in leaf dry weight (ΔQ_{leaf}) and the maximum specific leaf area (SLA_{max}):

$$\Delta \mathrm{LAI}_{d,c} = \Delta Q_{leaf} \times \mathrm{SLA}_{max}\,. \tag{S49}$$

Here, ΔQ_{leaf} also represents daily increment in leaf biomass which can be expressed as:

$$\Delta Q_{leaf} = \Delta Q \times F_{leaf}, \tag{S50}$$

where the actual daily biomass accumulation (ΔQ) results from water limitation applied on the potential radiation-driven biomass accumulation (ΔQ_r). Hence, when soil water is assumed to be non-limiting, biomass accumulation will be limited by the radiation:

$$\Delta Q = \Delta Q_r. \tag{S51}$$

Here, F_{leaf} denotes the fraction of available biomass partitioned to the leaf, which is defined as a function of the stage code (Supplementary Figure 2a,b). SLA_{max}, a function of LAI, can be calculated by the crop-specific SLA_{max}-LAI curve as shown in Supplementary Figures 2c. Similar to F_{leaf}, RUE (g/MJ) is intricately linked with the stage code (Supplementary Figure 2d).

The diffuse factor f_d can be expressed as[31]:

$$f_d = \frac{R_d}{R_s}, \tag{S52}$$

where R_d and R_s denote the daily diffused and global solar irradiance at the surface, respectively. These values will be accurately determined by our solar model, which operates at an advanced computing resolution of approximately 0.1 m based on the AV farm scale. Both the stress factor (f_s) and carbon dioxide factor (f_c) are set to 1 according to the present assumptions. In addition, recent field research has established a correlation between the harvest index (HI) and the seasonal average temperature[32]:

$$\text{HI} = -0.0072T_s^2 + 0.32T_s - 2.96\,, \tag{S53}$$

where T_s represents the growing season average canopy temperature.

Regarding the phenology of soybean (Supplementary Figure 2a), the timing of each phase, excluding the sowing-to-germination phase driven by sowing depth and thermal time, is determined by the accumulation of thermal time (TT), adjusted for other factors (like photoperiod) which vary with the phase considered. The length of each phase is dictated by a fixed thermal time target which is typically cultivar specific. During the computation of TT, the daily thermal time (ΔTT) can be calculated from the daily average of maximum and minimum crown temperatures (Supplementary Figure 2e)[29] for both Vegetative and Reproductive phases:

$$\Delta\text{TT} = \begin{cases} T_c - 10, & 10 \le T_c < 30 \\ 2(40 - T_c), & 30 \le T_c < 40 \\ 0, & T_c < 10 \text{ or } T_c \ge 40 \end{cases} \quad \text{(Vegetative Phase)}. \tag{S54}$$

$$\Delta\mathrm{TT} = \begin{cases} 5, & 10 \le T_c < 15 \\ 5 + (T_c - 15), & 15 \le T_c < 30 \\ 2(40 - T_c), & 30 \le T_c < 40 \\ 0, & T_c < 10 \text{ or } T_c \ge 40 \end{cases} \quad \text{(Reproductive Phase).} \tag{S55}$$

Here, T_c is the daily crown mean temperature which can be calculated by the maximum ($T_{c,max}$) and minimum ($T_{c,min}$) crown temperatures[33]:

$$T_c = \frac{T_{c,max} + T_{c,min}}{2}. \tag{S56}$$

Here, $T_{c,max}$ and $T_{c,min}$ can be computed based on the maximum (T_{max}) and minimum (T_{min}) air temperatures, respectively:

$$T_{c,max} = \begin{cases} 2 + T_{max}(0.4 + 0.0018(H_{snow} - 15)^2), & T_{max} < 0 \\ T_{max}, & T_{max} \ge 0 \end{cases}, \tag{S57}$$

$$T_{c,min} = \begin{cases} 2 + T_{min}(0.4 + 0.0018(H_{snow} - 15)^2), & T_{min} < 0 \\ T_{min}, & T_{min} \ge 0 \end{cases}, \tag{S58}$$

where H_{snow} is the snow depth which is set to zero in the present soybean model.

Meanwhile, the rate of thermal time accumulation was further modified by photoperiod modifier during the phase from end of the juvenile stage to floral initiation:

$$p_{m,D} = \frac{1}{6.76}(21.19 - p_{h,D}). \tag{S59}$$

Here, $p_{m,D}$ represents the daily photoperiod modifier, and $p_{h,D}$ denotes the duration of the day (in hours). Finally, the thermal time (TT) can be expressed as the sum of daily thermal times (ΔTT) over a specified number of days (n):

$$\mathrm{TT} = \sum_{D=1}^{n}(\Delta\mathrm{TT} \cdot p_{m,D}), \tag{S60}$$

where n is the number of days (D) for the accumulation of the thermal time.

Validation of the soybean model. To validate the simplified soybean model, we conducted a thorough comparative analysis against USDA NASS county-level historical soybean yields[34] from three distinct locations: Champaign, Illinois (40.0692° N, 88.2481° W), Faribault, Minnesota (44.2966° N, 93.2418° W), Bolivar, Mississippi (33.6566° N, 91.0464° W). The results, presented in Supplementary Figure 2f-h, underscore the robust performance of our soybean model. Most of our simulation results can be found to fall within ±6% of the actual field yields over the past 7 years (2016-2022), with a minority of cases exhibiting slight variances up to ±8%. The temporal trends of the simulated yields align closely with historical data, which underscores the model's capability to predict yields and capture the effects of variable climate conditions on annual soybean production. This alignment not only confirms the model's efficacy in forecasting soybean yields, but also highlights its utility in investigating the impacts of PV panel shading on soybean growth. Whin this context, the validated soybean model holds promise for applications in assessing the impact of solar installations on soybean performance, contributing valuable insights to sustainable agriculture practices in varying environmental contexts based on AV scenarios.

Supplementary Note 3

Economic model. On the agricultural side, the expected average annual soybean profit per unit AV farm area ($P_{crop,AV}$) can be expressed as:

$$P_{crop,AV} = \frac{O_{crop,AV}(\mathrm{PRI}_{crop} - \mathrm{VC}_{crop}) - \mathrm{FC}_{crop} A_{crop,AV}}{A_{AV}}, \quad \text{(S61)}$$

Here, $O_{crop,AV}$ denotes the crop (soybean) output (in bushels) of the AV system, PRI_{crop} represents the crop price (in US$/bushel), VC_{crop} indicates the variable cost of the crop (in US$/bushel), FC_{crop} is the fixed cost of the crop (in US$/acre), $A_{crop,AV}$ signifies the crop area (in acres) in the AV system, and A_{AV} represents the overall AV farm area (in acres). Similarly, the crop profit of a traditional crop farm ($P_{crop,farm}$, in US$/acre) can be calculated by:

$$P_{crop,farm} = \frac{O_{crop,farm}(\mathrm{PRI}_{crop} - \mathrm{VC}_{crop}) - \mathrm{FC}_{crop} A_{crop,farm}}{A_{crop,farm}}, \quad \text{(S62)}$$

where $O_{crop,farm}$ denotes the crop (soybean) output (in bushels) of a traditional crop farm, and $A_{crop,farm}$ represents the traditional crop farm area (in acres) equivalent to the AV system area (A_{AV}).

On PV energy side, the expected average annual PV profit per unit AV system area ($P_{e,AV}$) is defined as:

$$P_{e,AV} = (\mathrm{PPA} + \mathrm{REC} - \mathrm{LCOE}) E_{PV,i}\,, \quad \text{(S63)}$$

where PPA is the power purchase agreement (PPA) price of PV electricity (in US$/kWh), REC represents the solar renewable energy credit (in US$/kWh), LCOE denotes the levelized cost of energy for PV electricity (in US$/kWh), and $E_{PV,i}$ signifies the annual PV electricity generation (in kWh) in year i. Here, LCOE serves as a metric gauging the average net present cost of electricity generation throughout the lifespan of a generator, including PV and AV systems[35–37]. Acting as a valuable tool, LCOE facilitates a comprehensive comparison of the economic viability among diverse energy sources. This metric proves instrumental in conducting a cost-effectiveness assessment for energy generation technologies, especially pertinent to long-term evaluations of PV and AV systems[38–40]. The calculation of LCOE involves dividing the discounted sum of energy generation costs, encompassing capital expenditure, operating expenditure, land lease, and transmission costs, by the discounted total PV electricity production over the entire lifespan of the AV system[39,40]:

$$\mathrm{LCOE} = \frac{\mathrm{CAPEX}+\mathrm{NPV}\left((\mathrm{OPEX}_i+\mathrm{Lease}_i+\mathrm{Trans}_i)*(1+\mathrm{Inf})^{i-1},\forall i=1 \ldots T|\delta,T\right)}{\mathrm{NPV}\left(E_{PV,i}*(1-D)^{i-1},\forall i=1 \ldots T|\delta,T\right)}, \quad \text{(S64)}$$

Here, CAPEX represents the capital expenditure, OPEX_i denotes the annual operating expenditure, Lease_i reflects the annual land lease cost, and Trans_i signifies the annual transmission cost in year i. The variable i designates the specific year under consideration. Additionally, Inf denotes the inflation rate, D represents the annual degradation rate of PV modules, δ is the real discount rate, T signifies the economic life of the AV system, and NPV stands for the net present value[41,42].

In Supplementary Table 2, a comprehensive depiction of the parameters employed in the economic model is presented. The current AV system boasts a 25-year lifespan, accompanied by an annual operating expense (OPEX) of US$15/kW. Leveraging outputs from our solar and crop models, which compute PV generation and crop yield respectively, these vital data are seamlessly integrated into our economic model. This meticulous integration facilitates a systematic modelling procedure encompassing PV generation, crop yield, and economic profit, thereby enhancing the comprehensiveness of the AV implementation analysis.

Supplementary Note 4

Optimization model. NSGA-II[43–45] operates on four foundational principles: Non-Dominated Sorting, Elite Preserving Operator, Crowding Distance and Selection Operator, as illustrated in Fig. 2c and Supplementary Figure 14.

The Non-Dominated Sorting is the initial step, where the algorithm sorts the population based on Pareto dominance. During Non-Dominated Sorting, the population members are sorted using the concept of Pareto dominance. Initially, the algorithm assigns the highest priority (first rank) to the non-dominated individuals within the population, segregating them into the foremost front and subsequently removing them from consideration for the current sorting phase. This procedure iterates, with each cycle identifying the next set of non-dominated members, assigning them a subsequent rank, and placing them in the next front, until all individuals are ranked, as depicted Supplementary Figure 14b.

The Elite Preserving Operator ensures the retention of elite solutions across generations, transferring non-dominated solutions from one generation to the next unless they are outperformed by newer solutions.

The Crowding Distance measures the solution density surrounding a particular individual, which is calculated as the average distance between two nearest solutions for each objective along the Pareto Front Approximation. This metric helps maintain diversity by favoring individuals in less crowded regions as indicated by large crowding distance. The crowding distance for an individual is depicted through the average side-length of the cuboid formed by its neighboring solutions, as demonstrated in Supplementary Figure 14c, and mathematically represented by the formula in equation (S65):

$$\mathrm{CD}(i) = \sum_{i=1}^{k} \frac{f_j^{i+1} - f_j^{i-1}}{f_j^{max} - f_j^{min}}, \tag{S65}$$

where $\mathrm{CD}(i)$ denotes the crowding distance for the i^{th} individual, f_j^{max} and f_j^{min} are the maximum and minimum values of the j^{th} objective function across all individuals, and k is the number of objectives.

The Selection Operator guides the formation of the subsequent generation's population through crowded tournament selection, leveraging both the ranks and crowding distances of individuals. The selection criteria prioritize individuals of superior rank; among those of equal rank, individuals with greater crowding distances are chosen, which ensures both quality and diversity in the evolving population.

To facilitate the seamless implementation of Multi-Objective Optimization Design (MOOD) within our AV system, we integrated jMetalPy[46], an open-source Python-based framework tailored for multi-objective optimization algorithms, into our AV system model. To strike a balance between computational load and solution diversity, we set the population size to 100, which allows for a broad exploration of solutions while managing computational resources efficiently. The population size determines the number of solutions (individuals) in each generation. The same size was applied to the offspring population to ensure a steady population count across generations. For mutation, we chose PolynomialMutation with its probability set as the reciprocal of the number of variables. This ensures that the mutation rate inversely scales with the number of variables, thus enhancing diversity without saturating the search space. We set the distribution index to 20 to properly control the mutation's spread within the population. We employed the Simulated Binary Crossover (SBXCrossover) as the crossover operator for real-valued variables. In SBXCrossover, we set the probability to 1.0, which indicates that crossover occurs in every pair of selected solutions. The distribution index was similarly set at 20 for the crossover operator, which influences offspring distribution to favor solutions nearer to their parents, thus enabling thorough local searches. Finally, we set the convergence condition of NSGA-II based on the average change in the spread of Pareto solutions ($\Delta\mathrm{SPS}_g$)[47], which is calculated by:

$$\Delta\mathrm{SPS}_g = \left(\frac{\sum_{p=1}^{n(n-1)/2} d_{ij}}{n(n-1)/2}\right)_g - \left(\frac{\sum_{p=1}^{n(n-1)/2} d_{ij}}{n(n-1)/2}\right)_{g-1}, \tag{S66}$$

$$d_{ij} = \sqrt{\left(y_i - y_j\right)^2 + \left(x_i - x_j\right)^2}, \tag{S67}$$

Here, g represents the current iteration number. n denotes the total number of individuals in the population. i and j signify the indices ranging from 1 to n, with $i \neq j$ and $i < j$. d_{ij} refers to the span length (Euclidean distance) between any two solutions i and j along the Pareto-optimal front. The algorithm aims for convergence when $|\Delta\mathrm{SPS}_g| < 1E-3$, which indicates minimal disparity in Pareto solution spreads between successive iterations and suggesting an approach towards the true Pareto Front. Our MOOD results demonstrate that the Pareto solutions tend to converge within 100 iterations. To further explore the evolutionary process of MOOD, we extended the optimization to run for up to 1000 iterations, as detailed in Supplementary Video 4. This approach not only demonstrates the convergence behavior of our model but also enriches our understanding of the MOOD process over a more extended series of iterations.

Supplementary Figures

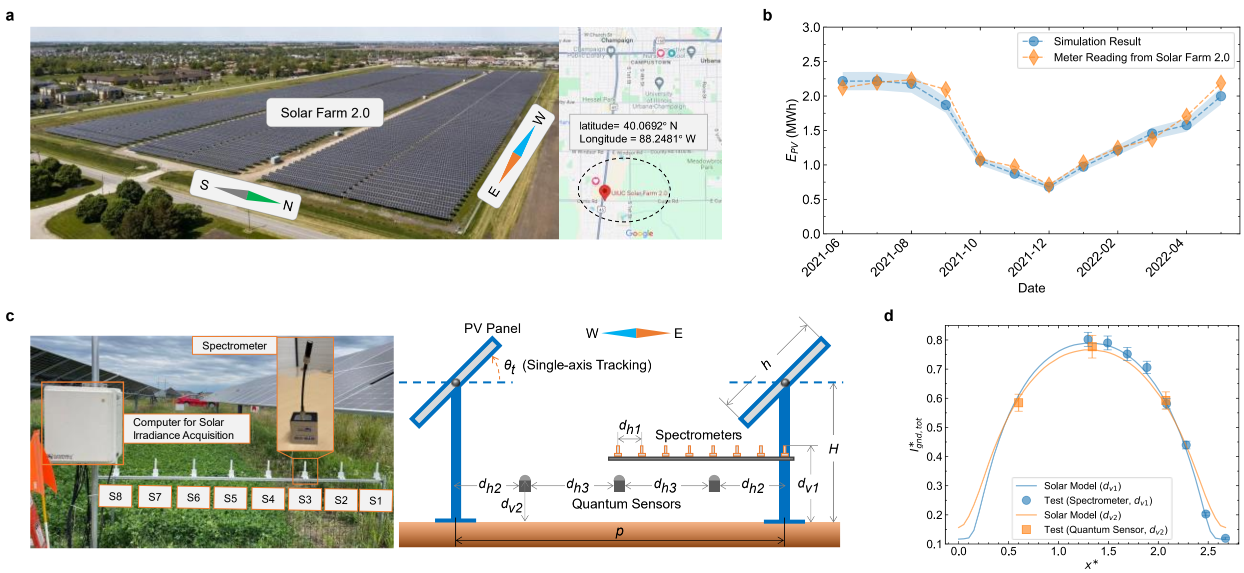

Supplementary Figure 1. Validation of the solar model. a, Three-dimensional view of Solar Farm 2.0, located in Champaign, Illinois (40.0692 ° N, 88.2481 ° W), featuring bi-facial monocrystalline PV panels equipped with dynamic east-west tracking system. **b**, Comparison of monthly (from June 2021 to May 2022) PV electricity generation (E_{PV}) between the solar modeling results (blue circles) and the meter readings (orange diamonds) from Solar Farm 2.0. The shaded blue area indicates the $\pm 6\%$ range around the simulation results, underscoring the model's accuracy. **c**, Schematic depicting the solar test setup at Solar Farm 2.0. Nine spectrometers (STS-VIS, $\pm 2\%$, Ocean Insight) are used for the dynamic Photosynthetically Active Radiation (PAR) capture, with eight installed at an interval (d_{h1}) of 0.39 m and a height (d_{v1}) of 0.84 m above the ground, and one beyond the confines of Solar Farm 2.0 to record the unobstructed PAR. Four quantum sensors (SQ-215-SS, $\pm 5\%$, Apogee Instruments) are deployed for additional PAR measurements. Three are mounted at a height (d_{v2}) of 0.69 m, with horizontal distances $d_{h2} = 1.20$ m and $d_{h3} = 1.52$ m, and one is positioned outside Solar Farm 2.0 to record the unobstructed PAR. **d**, Comparison of solar irradiance distribution ($I^*_{gnd,tot}$) between the solar modeling results (blue line and orange line) and the test outcomes (blue circles and orange squares). The blue color represents the $I^*_{gnd,tot}$ distribution at a height of d_{v1}, while the orange color denotes $I^*_{gnd,tot}$ distribution at a height of d_{v2}.

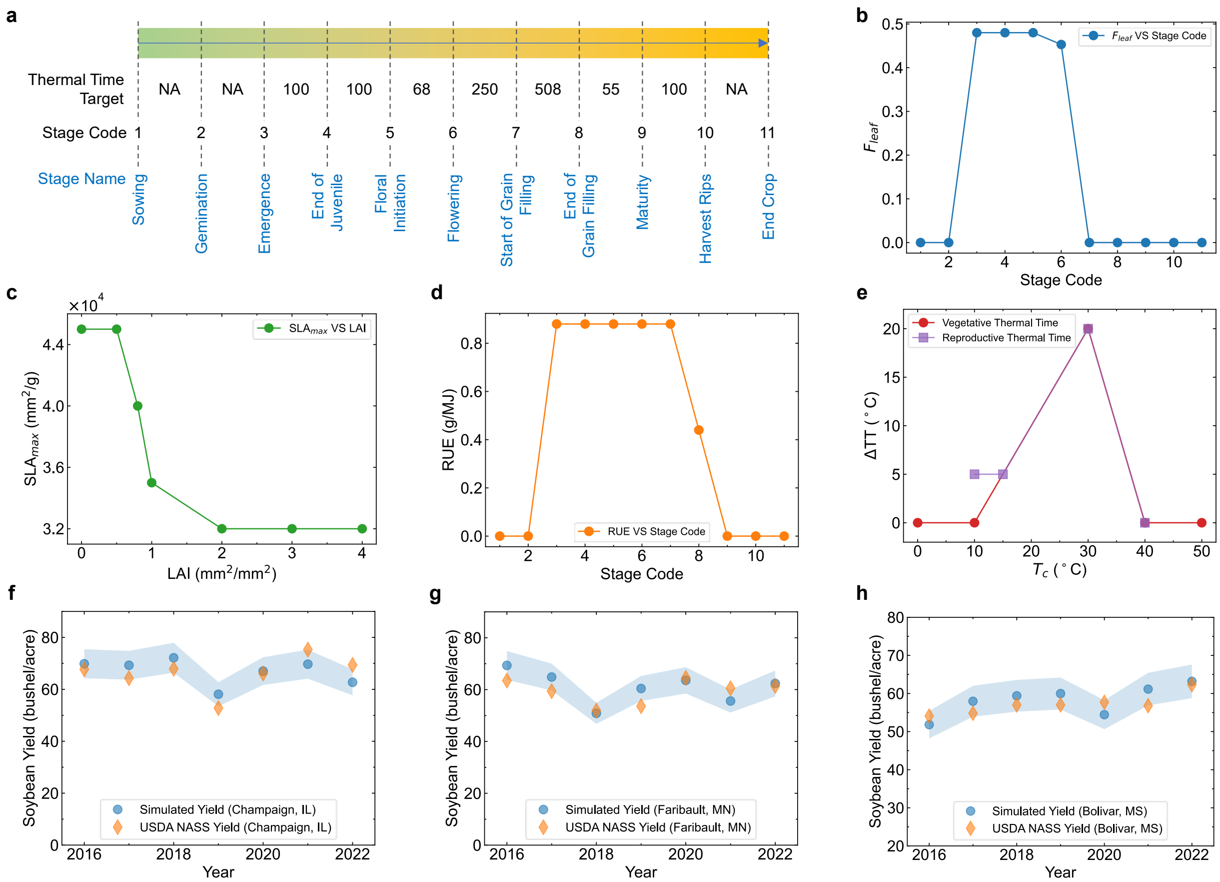

Supplementary Figure 2. Validation of the crop model. a, Conceptual diagram for phenological stages in the APSIM model, featuring thermal time target, phenological stage code and stage name. **b**, Relationship between F_{leaf} and the stage code. F_{leaf} denotes the fraction of available biomass partitioned to the leaf. **c**, Relationship between the maximum specific leaf area (SLA$_{max}$) and the leaf area index (LAI). **d**, Relationship between the radiation use efficiency (RUE) and the stage code. **e**, Relationship between the daily thermal time (ΔTT) and the daily crown mean temperature (T_c) for Vegetative and Reproductive Photoperiods, respectively. **f-h**, Comparison of soybean yield ($Y_{crop,farm}$) between the crop modeling results (blue circles) and the county-level historical yields (orange diamonds) sourced from the National Agricultural Statistics Service (NASS) of the United States Department of Agriculture (USDA). The sites compared include Champaign, Illinois (**f**), Faribault, Minnesota (**g**) and Bolivar, Mississippi (**h**), respectively. The shaded blue area denotes a ±8% range around the simulation results.

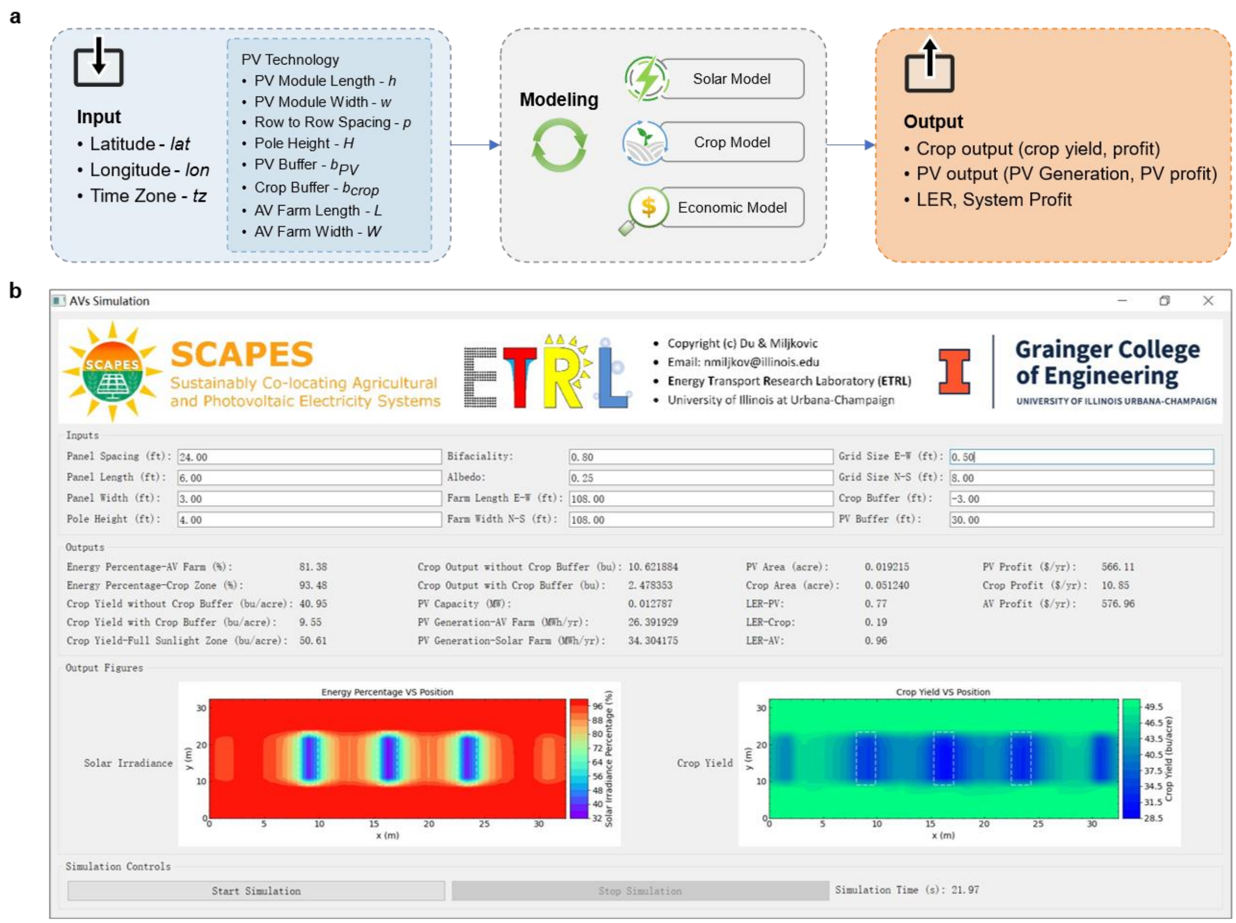

Supplementary Figure 3. Development of a Graphical User Interface (GUI) for AV system simulation based on python. a, Flowchart illustrating the sequential process of the AV system simulation, including the input parameters, modeling steps, and generated outputs. **b**, Basic layout of the GUI, featuring distinct modules for input, output, figure output, and simulation control. The input module allows users to specify AV design parameters, such as PV and farm dimensions, and PV technology specifications. The simulation control module, equipped with start and stop buttons, manages the simulation process, and indicates the completion time. The output module provides critical data on solar irradiance, crop yield, PV generation, Land Equivalent Ratio (LER), and overall system profitability. The figure output module visually represents solar irradiance and crop yield distributions across various pitches, tailored to the configured AV system specifications.

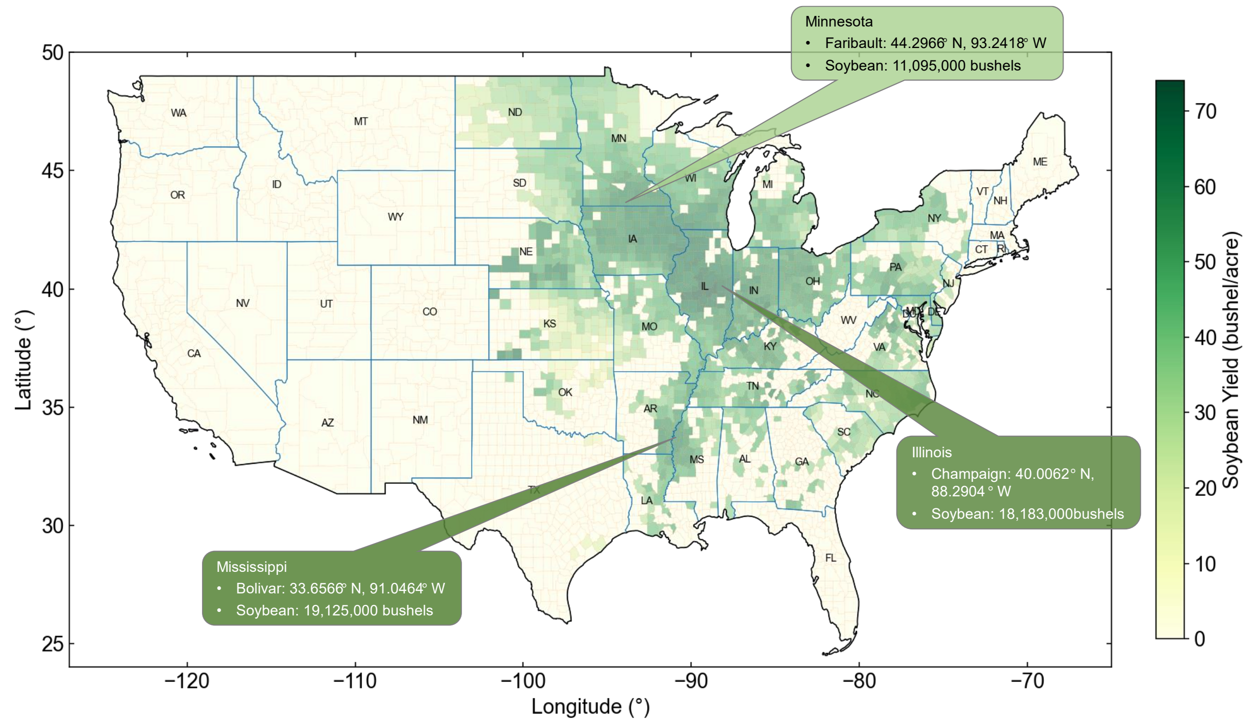

Supplementary Figure 4. Soybean yields by county in 2022 across selected US states. This map highlights the soybean yield data collected from the primary soybean production regions in the United States, including the Upper Midwest, the Northern Great Plains, and the Delta Region, among others. The data collection emphasizes areas known for significant soybean cultivation, offering insights into regional yield variations.

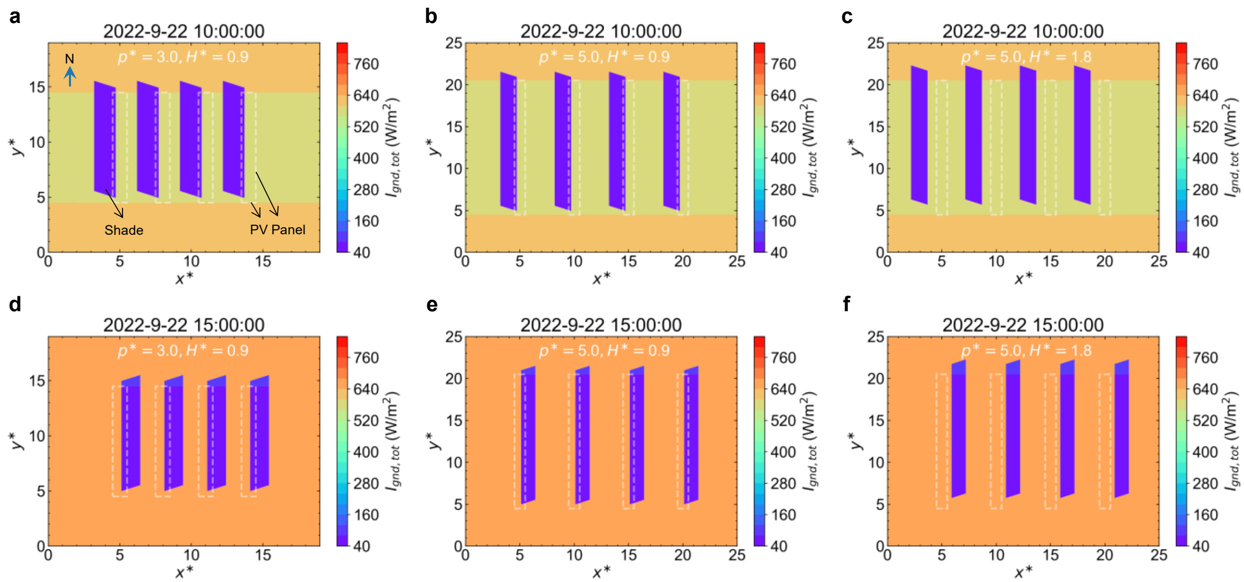

Supplementary Figure 5. Influence of row-to-row spacing ($\boldsymbol{p^*}$) and PV installation height ($\boldsymbol{H^*}$) on solar irradiance distribution ($\boldsymbol{I_{gnd,tot}}$) on AV farms. a-c, Contour of $I_{gnd,tot}$ at 10 am on September 22, 2022, for $p^* = 3$ and $H^* = 0.9$ (**a**), for $p^* = 5$ and $H^* = 0.9$ (**b**), and for $p^* = 5$ and $H^* = 1.8$ (**c**). **d-f**, Contour of $I_{gnd,tot}$ at 3 pm on September 22, 2022, for $p^* = 3$ and $H^* = 0.9$ (**d**), for $p^* = 5$ and $H^* = 0.9$ (**e**), and for $p^* = 5$ and $H^* = 1.8$ (**f**). The white dashed line represents the PV panel edge at zero tilt. Low $I_{gnd,tot}$ regions indicate the shaded areas under the PV panels. x^* and y^* signify the coordinates of the observation position on an AV farm, nondimensionalized by the PV module length (h). Both the row-to-row spacing (p^*) and the PV installation height (H^*) are nondimensionalized by h.

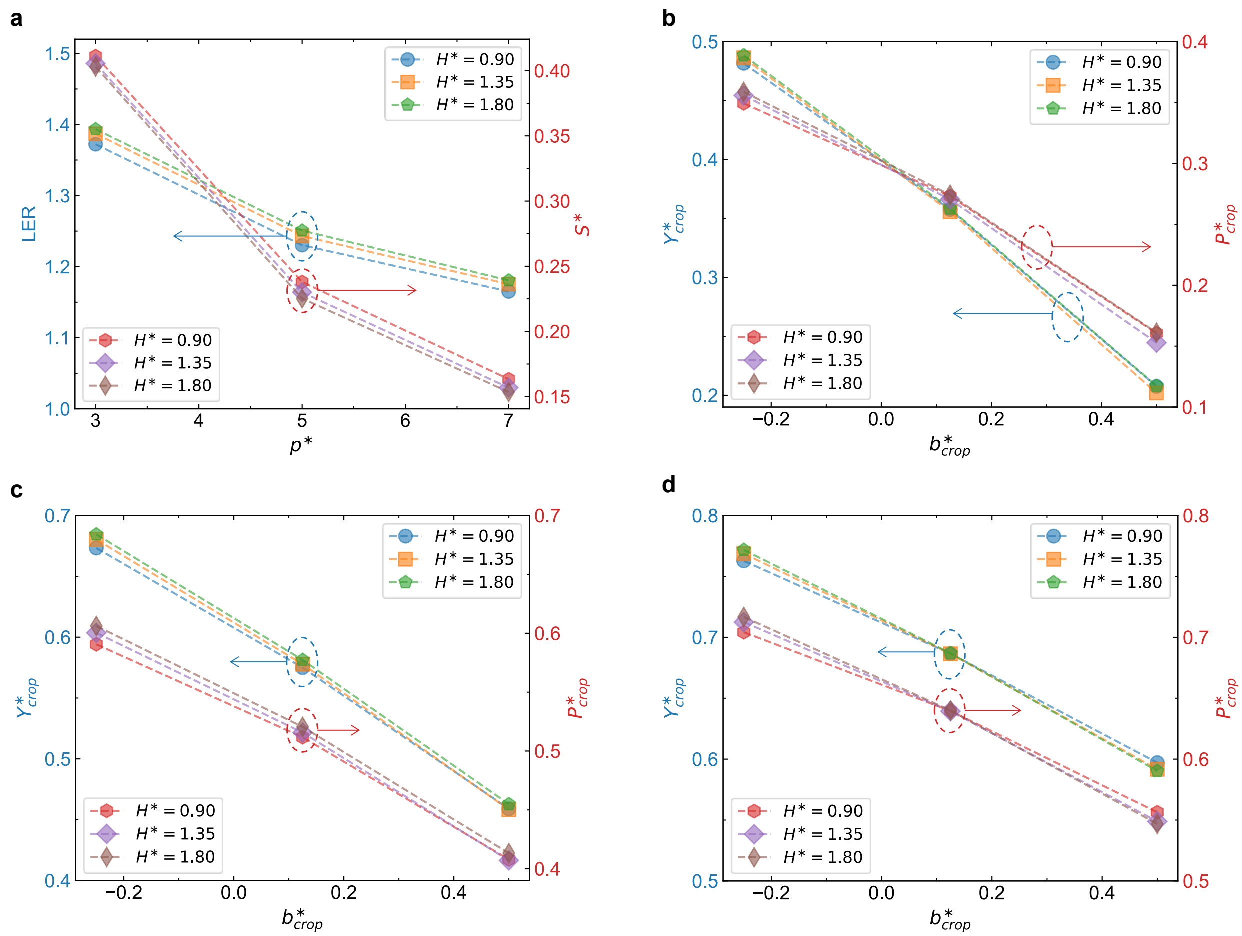

Supplementary Figure 6. Sensitivity analysis of design variables to PV and crop outputs based in an AV system. **a**, Influence of row-to-row spacing (p^*, pitch) on Land Equivalent Ratio (LER) and shade effect (S^*) across various PV installation heights (H^*). p^* and H^* refer to the row-to-row spacing and PV installation height nondimensionalized by the PV module length (h), respectively. Blue circles, orange squares and green pentagons, corresponding to H^* of 0.90, 1.35 and 1.80, respectively, demonstrate the correlation between LER and p^*. Red hexagons, violet diamonds, and thin brown diamonds, corresponding to H^* of 0.90, 1.35 and 1.80, illustrate the correlation between S^* and p^*. **b-d**, Influence of crop buffer (b^*_{crop}) on crop yield (Y^*_{crop}) and crop profit (P^*_{crop}) for varying row-to-row spacings: $p^* = 3$ in (**b**), 5 in (**c**) and 7 in (**d**), all under the same PV installation heights (H^*) as outlined in (**a**).

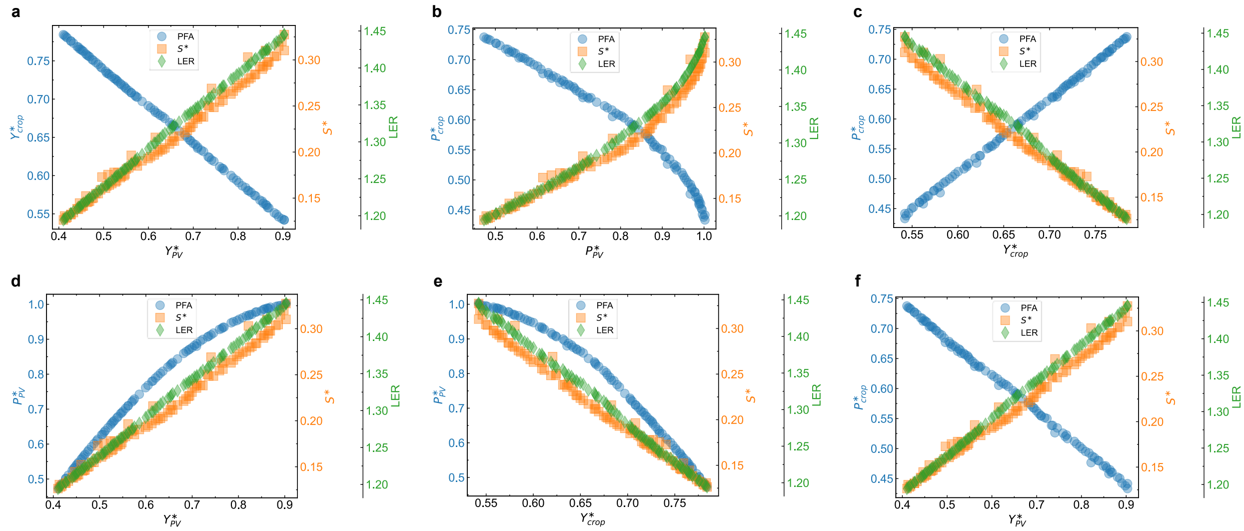

Supplementary Figure 7. Pareto Front Approximation (PFA) analysis utilizing the Non-dominated Sorting Genetic Algorithm (NSGA-II) in Faribault, Minnesota. a, Y_{PV}^{*} vs. Y_{crop}^{*}, Y_{PV}^{*} vs. S^{*}, and Y_{PV}^{*} vs. LER, illustrating how PV generation interacts with crop yield, shading impacts, and overall land use efficiency. **b**, P_{PV}^{*} vs. P_{crop}^{*}, P_{PV}^{*} vs. S^{*}, and P_{PV}^{*} vs. LER, illustrating how PV profit interacts with crop profit, shading impacts, and overall land use efficiency. **c**, Y_{crop}^{*} vs. P_{crop}^{*}, Y_{crop}^{*} vs. S^{*}, and Y_{crop}^{*} vs. LER, illustrating how crop yield interacts with crop profit, shading impacts, and overall land use efficiency. **d**, Y_{PV}^{*} vs. P_{PV}^{*}, Y_{PV}^{*} vs. S^{*}, and Y_{PV}^{*} vs. LER, illustrating how PV generation interacts with PV profit, shading impacts, and overall land use efficiency. **e**, Y_{crop}^{*} vs. P_{PV}^{*}, Y_{crop}^{*} vs. S^{*}, and Y_{crop}^{*} vs. LER, illustrating how crop yield interacts with PV profit, shading impacts, and overall land use efficiency. **f**, Y_{PV}^{*} vs. P_{crop}^{*}, Y_{PV}^{*} vs. S^{*}, and Y_{PV}^{*} vs. LER, illustrating how PV generation interacts with crop profit, shading impacts, and overall land use efficiency.

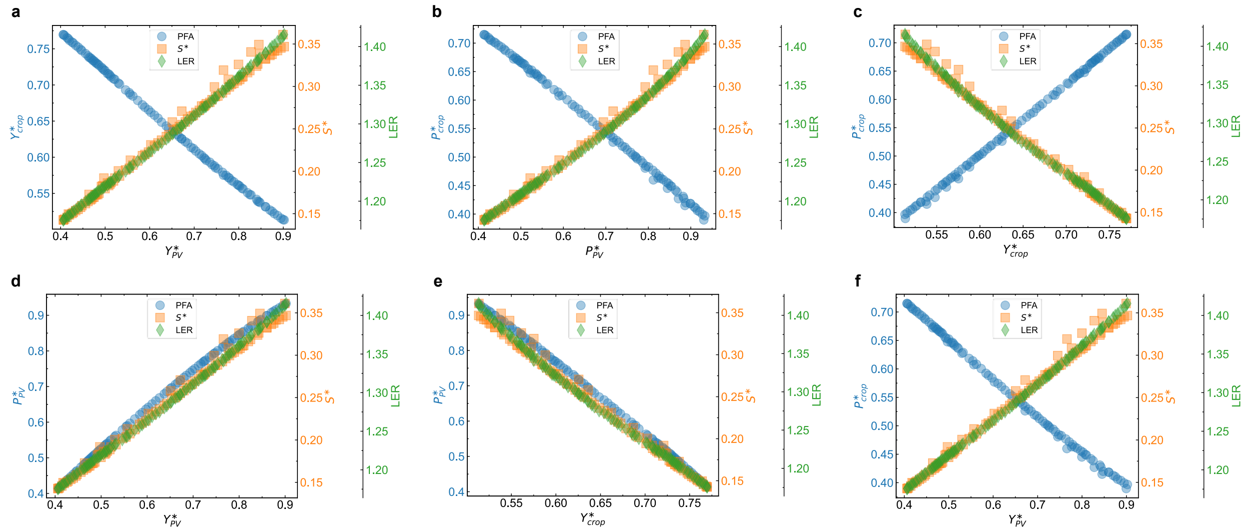

Supplementary Figure 8. Pareto Front Approximation (PFA) analysis utilizing the Non-dominated Sorting Genetic Algorithm (NSGA-II) in Bolivar, Mississippi. a, Y^*_{PV} vs. Y^*_{crop}, Y^*_{PV} vs. S^*, and Y^*_{PV} vs. LER, illustrating how PV generation interacts with crop yield, shading impacts, and overall land use efficiency. **b**, P^*_{PV} vs. P^*_{crop}, P^*_{PV} vs. S^*, and P^*_{PV} vs. LER, illustrating how PV profit interacts with crop profit, shading impacts, and overall land use efficiency. **c**, Y^*_{crop} vs. P^*_{crop}, Y^*_{crop} vs. S^*, and Y^*_{crop} vs. LER, illustrating how crop yield interacts with crop profit, shading impacts, and overall land use efficiency. **d**, Y^*_{PV} vs. P^*_{PV}, Y^*_{PV} vs. S^*, and Y^*_{PV} vs. LER, illustrating how PV generation interacts with PV profit, shading impacts, and overall land use efficiency. **e**, Y^*_{crop} vs. P^*_{PV}, Y^*_{crop} vs. S^*, and Y^*_{crop} vs. LER, illustrating how crop yield interacts with PV profit, shading impacts, and overall land use efficiency. **f**, Y^*_{PV} vs. P^*_{crop}, Y^*_{PV} vs. S^*, and Y^*_{PV} vs. LER, illustrating how PV generation interacts with crop profit, shading impacts, and overall land use efficiency.

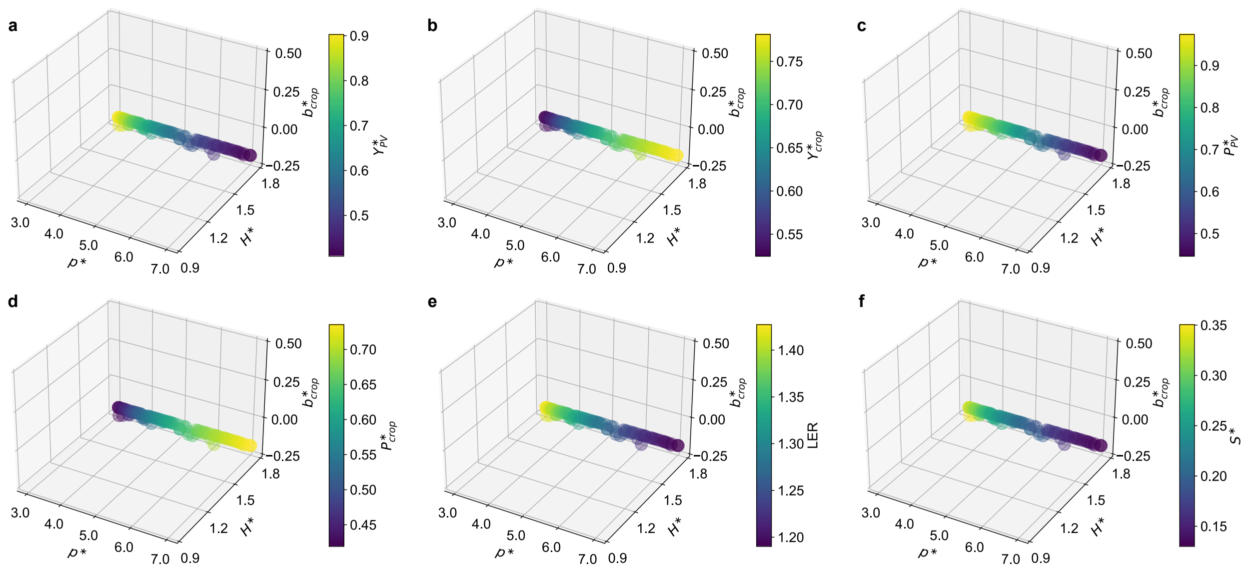

Supplementary Figure 9. Analysis of Pareto Set (PS) correlations with Agrivoltaic (AV) system objectives and key factors in Champaign, Illinois. This figure presents the relationships between the PS and each of the four AV objectives, including PV generation (Y_{PV}^{*}), PV profit (P_{PV}^{*}), crop yield (Y_{crop}^{*}), and crop profit (P_{crop}^{*}), alongside the shade effect (S^{*}) and the Land Equivalent Ratio (LER) within the optimal AV design variable domain. **a**, PS vs. Y_{PV}^{*}, demonstrating how variations in PS correlate with PV generation efficiency, guided by the color bar. **b**, PS vs. Y_{crop}^{*}, exploring the relationship between PS and crop yield, with the correlation strength indicated by the color bar. **c**, PS vs. P_{PV}^{*}, illustrating the correlation between PS and PV profit, as shown by the color bar. **d**, PS vs. P_{crop}^{*}, highlighting how PS influences crop profit, with the correlation degree represented by the color bar. **e**, PS vs. LER, examining the link between PS and LER, indicated by the color bar. **f,** PS vs. S^{*}, analyzing the correlation between PS and the shading effect with the impact magnitude shown by the color bar.

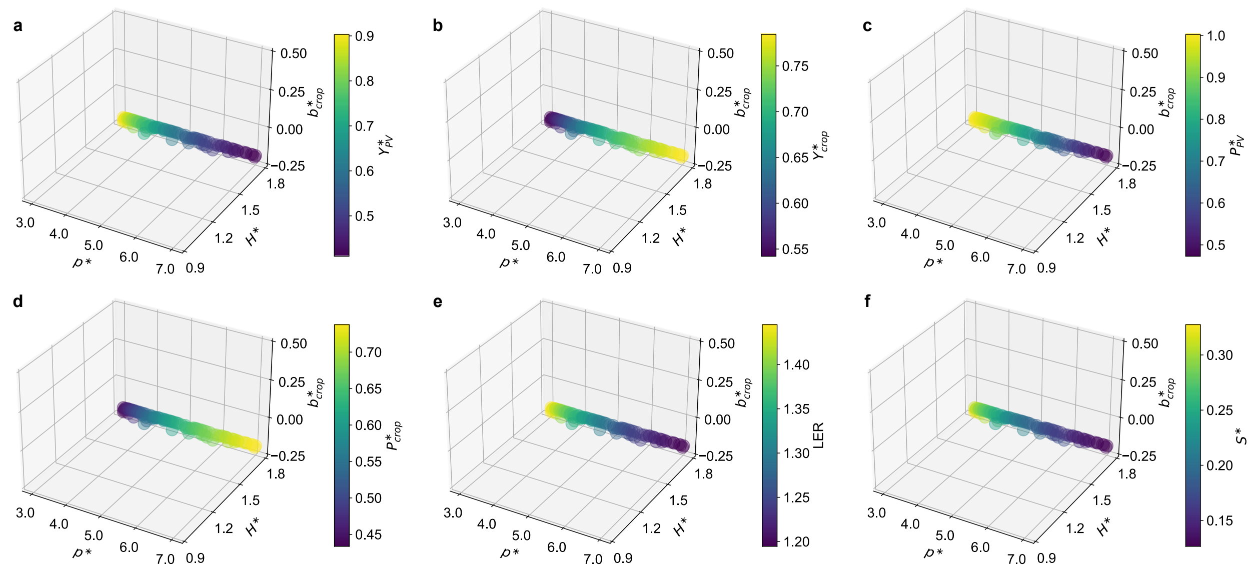

Supplementary Figure 10. Analysis of Pareto Set (PS) correlations with Agrivoltaic (AV) system objectives and key factors in Faribault, Minnesota. This figure presents the relationships between the PS and each of the four AV objectives, including PV generation (Y^*_{PV}), PV profit (P^*_{PV}), crop yield (Y^*_{crop}), and crop profit (P^*_{crop}), alongside the shade effect (S^*) and the Land Equivalent Ratio (LER) within the optimal AV design variable domain. **a**, PS vs. Y^*_{PV}, demonstrating how variations in PS correlate with PV generation efficiency, guided by the color bar. **b**, PS vs. Y^*_{crop}, exploring the relationship between PS and crop yield, with the correlation strength indicated by the color bar. **c**, PS vs. P^*_{PV}, illustrating the correlation between PS and PV profit, as shown by the color bar. **d**, PS vs. P^*_{crop}, highlighting how PS influences crop profit, with the correlation degree represented by the color bar. **e**, PS vs. LER, examining the link between PS and LER, indicated by the color bar. **f,** PS vs. S^*, analyzing the correlation between PS and the shading effect with the impact magnitude shown by the color bar.

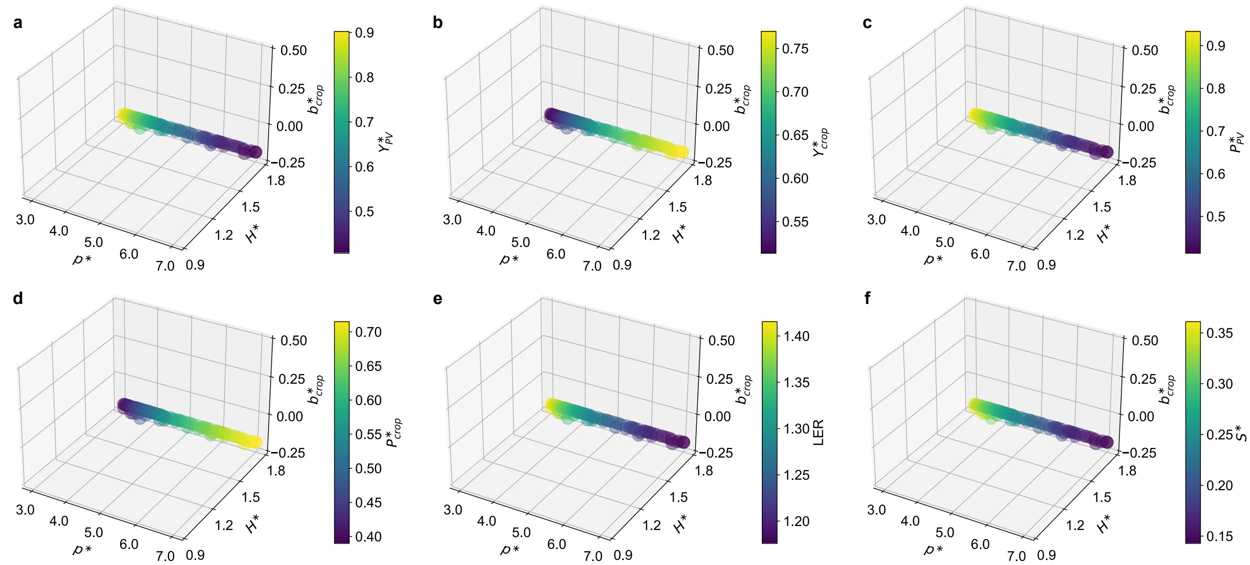

Supplementary Figure 11. Analysis of Pareto Set (PS) correlations with Agrivoltaic (AV) system objectives and key factors in Bolivar, Mississippi. This figure presents the relationships between the PS and each of the four AV objectives, including PV generation (Y^*_{PV}), PV profit (P^*_{PV}), crop yield (Y^*_{crop}), and crop profit (P^*_{crop}), alongside the shade effect (S^*) and the Land Equivalent Ratio (LER) within the optimal AV design variable domain. **a**, PS vs. Y^*_{PV}, demonstrating how variations in PS correlate with PV generation efficiency, guided by the color bar. **b**, PS vs. Y^*_{crop}, exploring the relationship between PS and crop yield, with the correlation strength indicated by the color bar. **c**, PS vs. P^*_{PV}, illustrating the correlation between PS and PV profit, as shown by the color bar. **d**, PS vs. P^*_{crop}, highlighting how PS influences crop profit, with the correlation degree represented by the color bar. **e**, PS vs. LER, examining the link between PS and LER, indicated by the color bar. **f,** PS vs. S^*, analyzing the correlation between PS and the shading effect with the impact magnitude shown by the color bar.

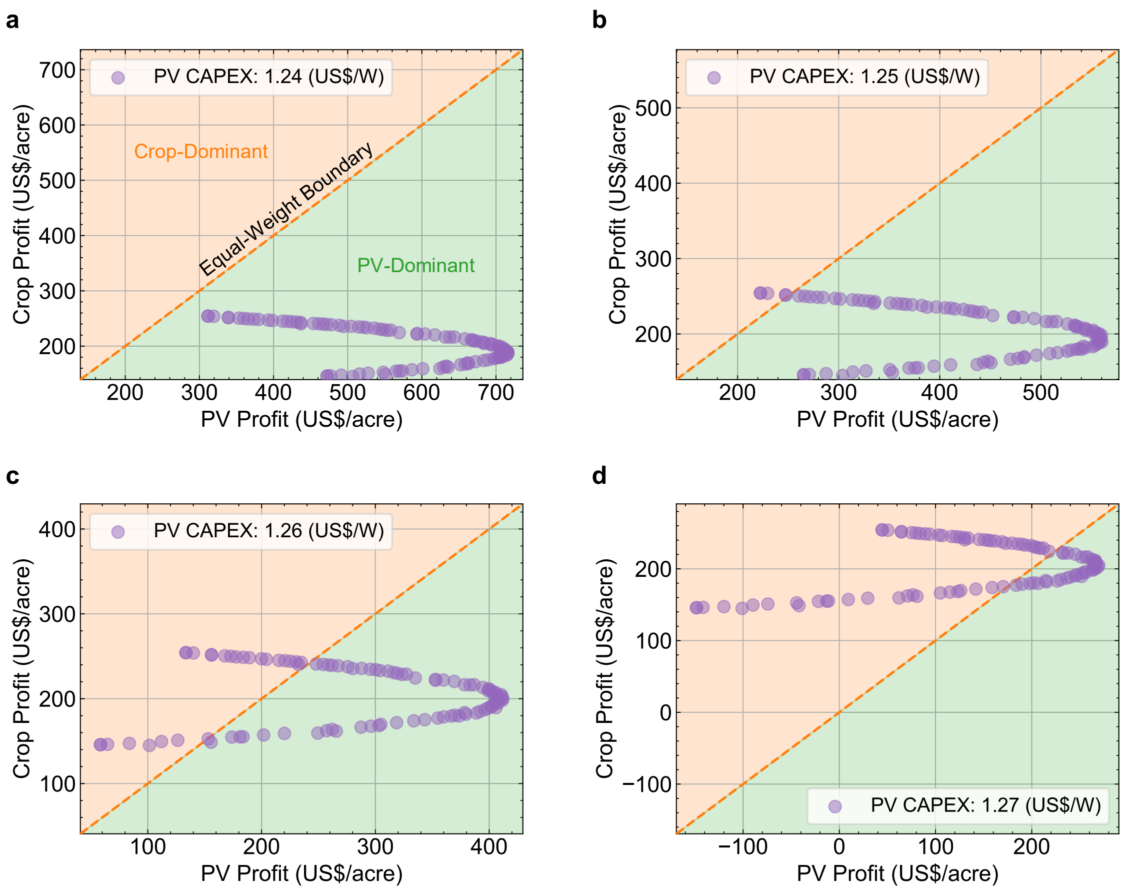

Supplementary Figure 12. Correlation between PV profit and crop profit per land area. This figure presents the optimal trade-off between the PV profit and the crop profit at various PV costs, referring to PV capital expenditure (CAPEX). **a**, PV CAPEX = 1.24 US$/W. **b**, PV CAPEX = 1.25 US$/W. **c**, PV CAPEX = 1.26 US$/W. **d**, PV CAPEX = 1.27 US$/W. The orange dotted line represents the equal-weight boundary between PV profit and crop profit, with the crop-dominant region above the boundary and the PV-dominant region below it.

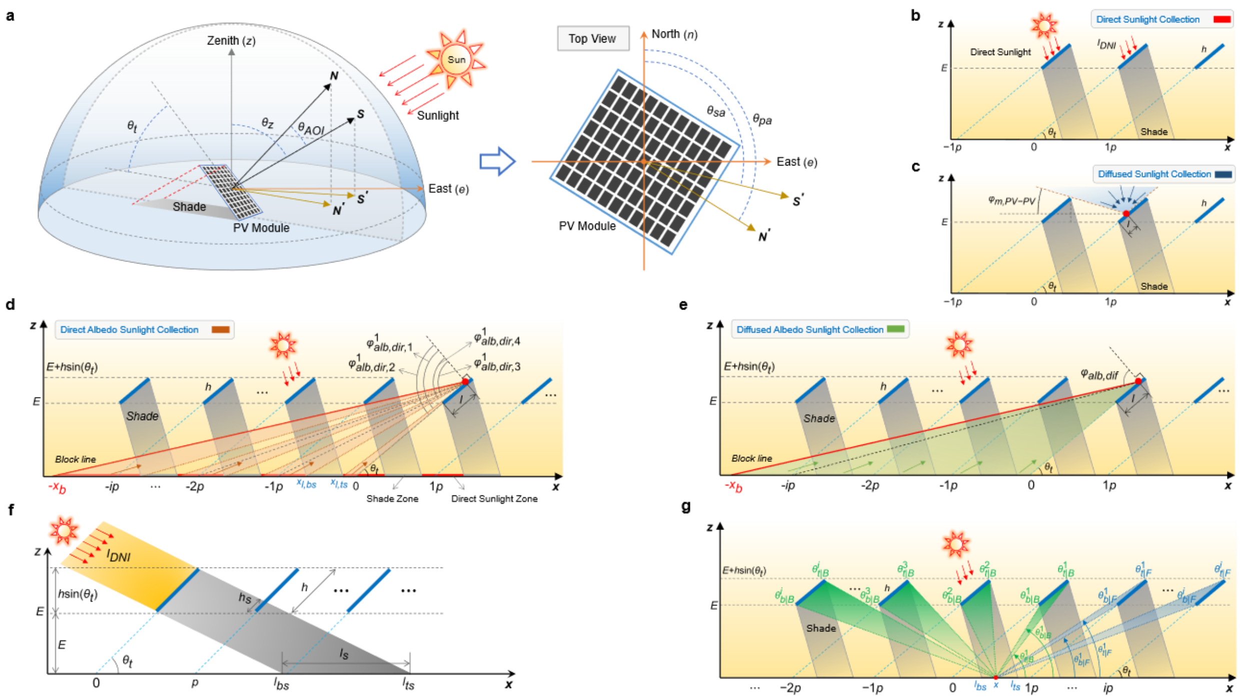

Supplementary Figure 13. Schematic of the solar model development. a, Schematic of the PV module's orientation in relation to the sun. **b**, Schematic of direct sunlight collection on the front surface of a PV panel. **c**, Schematic of diffused sunlight collection on the front surface of a PV panel. **d**, Schematic of direct albedo sunlight collection on the front surface of a PV panel. **e**, Schematic of diffused albedo sunlight collection on the front surface of a PV panel. **f**, Schematic of the shade cast by a PV panel under sunlight. **g**, Schematic of the diffused solar irradiance reaching an arbitrary observation point (x) on the ground or at any elevation within an AV farm.

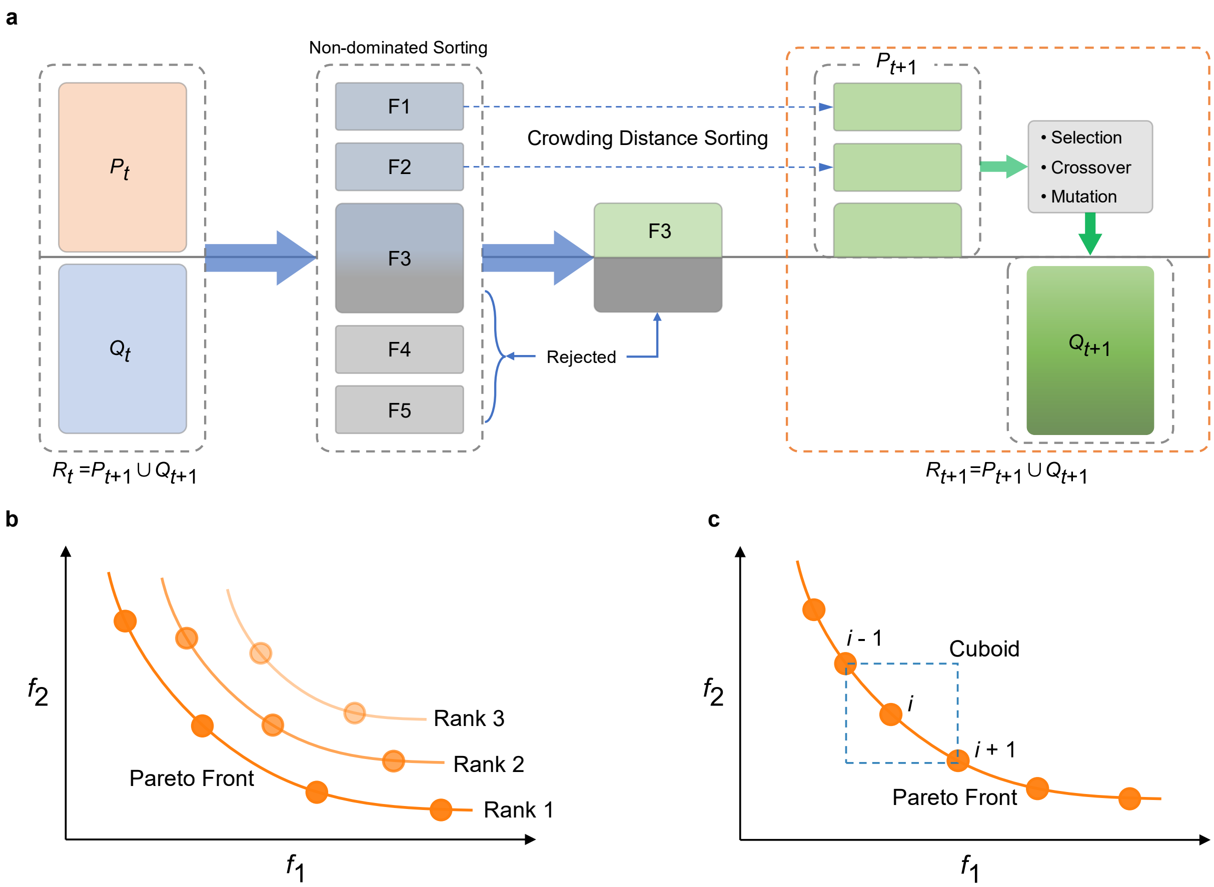

Supplementary Figure 14. Illustrative overview of the NSGA-II procedure. a, Flow chart demonstrating key steps of the NSGA-II algorithm, from initialization through to the selection of the next generation. **b**, Schematic of Non-dominated sorting procedure. **c**, Schematic of Crowding distance calculation.

Supplementary Tables

Supplementary Table 1. Main PV module specifications used in the solar model.

Electrical Data | STC*		**Nominal Max. Power (P_{max}, W)**	**Module Efficiency (%)**
Bifacial Module		365	18.2
Bifacial Gain**	5%	383	19.1
	10%	402	20.0
	20%	438	21.8
	30%	475	23.7
Operating Temperature		-40°C ~ +85°C	
Power Bifaciality***		70%	
Dimensions		2022 × 992 × 30 mm (79.6 × 39.1 × 1.18 in)	
Temperature Coefficient (P_{max})		-0.36%/°C	
Nominal Module Operating Temperature		41 ± 3°C	

* Under Standard Test Conditions (STC) of irradiance of 1000 W/m^2, spectrum AM 1.5 and cell temperature of 25°C.

** Bifacial Gain: The additional gain from the back side compared to the power of the front side at the standard test condition. It depends on mounting (structure, height, tilt angle etc.) and albedo of the ground.

*** Power Bifaciality = $P_{max,rear}/P_{max,front}$, both $P_{max,rear}$ and $P_{max,front}$ are tested under STC, Bifaciality Tolerance: ± 5%.

Supplementary Table 2. Parameters used in the economic model. CAPEX represents the capital expenditure, and OPEX denotes the operating expenditure.

Parameters	Variable	Units	Value
Solar Component			
Expected lifetime of PV/AV system[48,49]	T	years	25.00
Annual degradation rate of PV modules[48,49]	D	%/year	0.50
Real discount rate[48,49]	δ	%/year	6.50
Inflation rate[48–50]	Inf	%/year	2.50
Raised panel CAPEX[17,51]	CAPEX	US$/W	1.07
Annual OPEX for AV system[52,53]	OPEX_i	US$/kW	15.00
Annual transmission cost for PV electricity[54]	Trans_i	US$/MWh	3.67
Annual land lease cost for AV system[48,49]	Lease_i	US$/acre	1000.00
Power purchase agreement price of PV electricity[55]	PPA	US$/MWh	75.70
Solar renewable energy credit[56]	REC	US$/MWh	6.60
Agricultural component			
Soybean price[57]	PRI_{crop}	US$/bushel	9.69
Soybean Variable Cost[57]	VC_{crop}	US$/bushel	2.50
Soybean Fixed Cost[57]	FC_{crop}	US$/acre	136.00

Supplementary References

1. Jacobson, M. Z. *Fundamentals of Atmospheric Modeling*. (Cambridge university press, 1999).
2. Hartmann, D. L. *Global Physical Climatology*. vol. 103 (Newnes, 2015).
3. Bonan, G. Ecological climatology: concepts and applications. (2015).
4. Mahmoud, M., Olabi, A. G., Radwan, A., Yousef, B. A. & Abdelkareem, M. A. Case studies and analysis of solar thermal energy systems. in *Renewable Energy-Volume 1: Solar, Wind, and Hydropower* 75–92 (Elsevier, 2023).
5. Reda, I. & Andreas, A. Solar position algorithm for solar radiation applications. *Solar energy* **76**, 577–589 (2004).
6. Reda, I. & Andreas, A. Solar position algorithm for solar radiation applications (vol 76, pg 577, 2004). *Solar Energy* **81**, 838–838 (2007).
7. Anderson, K. & Mikofski, M. *Slope-Aware Backtracking for Single-Axis Trackers*. https://www.osti.gov/biblio/1660126 (2020).
8. Riaz, M. H., Imran, H., Younas, R., Alam, M. A. & Butt, N. Z. Module technology for agrivoltaics: Vertical bifacial versus tilted monofacial farms. *IEEE Journal of Photovoltaics* **11**, 469–477 (2021).
9. Patel, M. T., Khan, M. R., Sun, X. & Alam, M. A. A worldwide cost-based design and optimization of tilted bifacial solar farms. *Applied Energy* **247**, 467–479 (2019).
10. Mikofski, M. A., Darawali, R., Hamer, M., Neubert, A. & Newmiller, J. Bifacial performance modeling in large arrays. in *2019 IEEE 46th Photovoltaic Specialists Conference (PVSC)* 1282–1287 (IEEE, 2019).
11. Marion, B. *et al.* A practical irradiance model for bifacial PV modules. in *2017 IEEE 44th*

Photovoltaic Specialist Conference (PVSC) 1537–1542 (IEEE, 2017).

12. Markvart, T. *Practical Handbook of Photovoltaics: Fundamentals and Applications*. (Elsevier, 2003).
13. Faiman, D. Assessing the outdoor operating temperature of photovoltaic modules. *Progress in Photovoltaics* **16**, 307–315 (2008).
14. IEC. IEC 61853-3. Photovoltaic (PV) Module Performance Testing and Energy Rating—Part 3: Energy Rating of PV Modules. (2018).
15. Driesse, A., Stein, J. & Theristis, M. *Improving Common PV Module Temperature Models by Incorporating Radiative Losses to the Sky.* https://www.osti.gov/biblio/1884890 (2022).
16. Dobos, A. P. *PVWatts Version 5 Manual*. https://www.osti.gov/biblio/1158421 (2014).
17. Ramasamy, V., Feldman, D., Desai, J. & Margolis, R. *US Solar Photovoltaic System and Energy Storage Cost Benchmarks: Q1 2021*. https://www.osti.gov/biblio/1829460 (2021).
18. Sengupta, M., Weekley, A., Habte, A., Lopez, A. & Molling, C. *Validation of the National Solar Radiation Database (NSRDB)(2005-2012)*. https://www.osti.gov/biblio/1225344 (2015).
19. Sengupta, M. *et al. Physics-Based GOES Satellite Product for Use in NREL's National Solar Radiation Database*. https://www.osti.gov/biblio/1136571 (2014).
20. Habte, A., Sengupta, M. & Wilcox, S. *Validation of GOES-Derived Surface Radiation Using NOAA's Physical Retrieval Method*. https://www.osti.gov/biblio/1067900 (2013).
21. Habte, A., Sengupta, M. & Wilcox, S. Comparing measured and satellite-derived surface irradiance. in *Energy Sustainability* vol. 44816 561–566 (American Society of Mechanical Engineers, 2012).
22. Heidinger, A. K., Foster, M. J., Walther, A. & Zhao, X. T. The pathfinder atmospheres–

extended AVHRR climate dataset. *Bulletin of the American Meteorological Society* **95**, 909–922 (2014).

23. Pinker, R. T. & Laszlo, I. Modeling surface solar irradiance for satellite applications on a global scale. *Journal of Applied Meteorology and Climatology* **31**, 194–211 (1992).
24. Gomez-Casanovas, N. *et al.* Knowns, uncertainties, and challenges in agrivoltaics to sustainably intensify energy and food production. *Cell Reports Physical Science* (2023).
25. Avila, L., De Paula, M., Trimboli, M. & Carlucho, I. Deep reinforcement learning approach for MPPT control of partially shaded PV systems in Smart Grids. *Applied Soft Computing* **97**, 106711 (2020).
26. Pandey, O. P., Dung, V. V. D., Mishra, P. & Kumar, R. Simulating rooftop solar arrays with varying design parameters to study effect of mutual shading. *Energy for Sustainable Development* **68**, 425–440 (2022).
27. Keiner, D., Walter, L., ElSayed, M. & Breyer, C. Impact of backtracking strategies on techno-economics of horizontal single-axis tracking solar photovoltaic power plants. *Solar Energy* **267**, 112228 (2024).
28. Brown, H. E. *et al.* Plant modelling framework: software for building and running crop models on the APSIM platform. *Environmental Modelling & Software* **62**, 385–398 (2014).
29. Archontoulis, S. V., Miguez, F. E. & Moore, K. J. A methodology and an optimization tool to calibrate phenology of short-day species included in the APSIM PLANT model: application to soybean. *Environmental modelling & software* **62**, 465–477 (2014).
30. Robertson, M. J. & Carberry, P. S. Simulating growth and development of soybean in APSIM. (1998).
31. Roderick, M. L. Estimating the diffuse component from daily and monthly measurements of

global radiation. *Agricultural and Forest Meteorology* **95**, 169–185 (1999).

32. Burroughs, C. H. *et al.* Reductions in leaf area index, pod production, seed size, and harvest index drive yield loss to high temperatures in soybean. *Journal of experimental botany* **74**, 1629–1641 (2023).
33. Zheng, B., Chenu, K., Doherty, A. & Chapman, S. The APSIM-wheat module (7.5 R3008). *Agricultural Production Systems Simulator (APSIM) Initiative* **615**, (2014).
34. USDA - National Agricultural Statistics Service Homepage.
35. Lee, J. T. & Callaway, D. S. The cost of reliability in decentralized solar power systems in sub-Saharan Africa. *Nature Energy* **3**, 960–968 (2018).
36. Probst, B., Anatolitis, V., Kontoleon, A. & Anadón, L. D. The short-term costs of local content requirements in the Indian solar auctions. *Nature Energy* **5**, 842–850 (2020).
37. Sterl, S., Fadly, D., Liersch, S., Koch, H. & Thiery, W. Linking solar and wind power in eastern Africa with operation of the Grand Ethiopian Renaissance Dam. *Nature Energy* **6**, 407–418 (2021).
38. Bano, T. & Rao, K. V. S. Levelized electricity cost of five solar photovoltaic plants of different capacities. *Procedia Technology* **24**, 505–512 (2016).
39. Schindele, S. *et al.* Implementation of agrophotovoltaics: Techno-economic analysis of the price-performance ratio and its policy implications. *Applied Energy* **265**, 114737 (2020).
40. Agostini, A., Colauzzi, M. & Amaducci, S. Innovative agrivoltaic systems to produce sustainable energy: An economic and environmental assessment. *Applied Energy* **281**, 116102 (2021).
41. McKuin, B. *et al.* Energy and water co-benefits from covering canals with solar panels. *Nature Sustainability* **4**, 609–617 (2021).

42. Wang, Y. *et al.* Accelerating the energy transition towards photovoltaic and wind in China. *Nature* **619**, 761–767 (2023).
43. Verma, S., Pant, M. & Snasel, V. A comprehensive review on NSGA-II for multi-objective combinatorial optimization problems. *Ieee Access* **9**, 57757–57791 (2021).
44. Deb, K., Pratap, A., Agarwal, S. & Meyarivan, T. A fast and elitist multiobjective genetic algorithm: NSGA-II. *IEEE transactions on evolutionary computation* **6**, 182–197 (2002).
45. Deb, K., Agrawal, S., Pratap, A. & Meyarivan, T. A Fast Elitist Non-dominated Sorting Genetic Algorithm for Multi-objective Optimization: NSGA-II. in *Parallel Problem Solving from Nature PPSN VI* (eds. Schoenauer, M. et al.) vol. 1917 849–858 (Springer Berlin Heidelberg, Berlin, Heidelberg, 2000).
46. Benítez-Hidalgo, A., Nebro, A. J., García-Nieto, J., Oregi, I. & Del Ser, J. jMetalPy: A Python framework for multi-objective optimization with metaheuristics. *Swarm and Evolutionary Computation* **51**, 100598 (2019).
47. Sahu, S. N., Murmu, S. K. & Nayak, N. C. Multi-objective optimization of EDM process with performance appraisal of GA based algorithms in neural network environment. *Materials Today: Proceedings* **18**, 3982–3997 (2019).
48. Freeman, J. M. *et al. System Advisor Model (SAM) General Description (Version 2017.9. 5)*. https://www.osti.gov/biblio/1440404 (2018).
49. GitHub - NREL/SAM: System Advisor Model (SAM). https://github.com/NREL/SAM.
50. Maclaurin, G. *et al. The Renewable Energy Potential (reV) Model: A Geospatial Platform for Technical Potential and Supply Curve Modeling*. https://www.osti.gov/biblio/1563140 (2019).
51. Bolinger, M., Seel, J., Warner, C. & Robson, D. *Utility-Scale Solar, 2021 Edition: Empirical*

Trends in Deployment, Technology, Cost, Performance, PPA Pricing, and Value in the United States [Slides]. https://www.osti.gov/biblio/1823604 (2021).

52. Ramasamy, V. *et al. Us Solar Photovoltaic System and Energy Storage Cost Benchmarks, with Minimum Sustainable Price Analysis: Q1 2022*. https://www.osti.gov/biblio/1891204 (2022).
53. Ramasamy, V. *et al. US Solar Photovoltaic System and Energy Storage Cost Benchmarks, With Minimum Sustainable Price Analysis: Q1 2023*. https://www.osti.gov/biblio/2005540 (2023).
54. Lopez, A. *et al.* Land use and turbine technology influences on wind potential in the United States. *Energy* **223**, 120044 (2021).
55. Utility-Scale Solar 2023 PPAs. *Tableau Software* https://public.tableau.com/views/Utility-ScaleSolar2023PPAs/USSPPADB?:embed=y&:showVizHome=no&:host_url=https%3A%2F%2Fpublic.tableau.com%2F&:embed_code_version=3&:tabs=no&:toolbar=yes&:animate_transition=yes&:display_static_image=no&:display_spinner=no&:display_overlay=yes&:display_count=yes&:language=en-US&publish=yes&:loadOrderID=0.
56. U.S. Department of Energy. 2021. "The Solar Futures Study." NREL/FS-6A20-80826. National Renewable Energy Lab. (NREL), Golden, CO (United States). https://www.osti.gov/biblio/1820105-solar-futures-study.
57. USDA - National Agricultural Statistics Service Homepage. https://www.nass.usda.gov/.